

Numerical Heat Transfer, Part B: Fundamentals



An International Journal of Computation and Methodology

ISSN: 1040-7790 (Print) 1521-0626 (Online) Journal homepage: http://www.tandfonline.com/loi/unhb20

Transient Schemes for Capturing Interfaces of Free-Surface Flows

F. Moukalled & M. Darwish

To cite this article: F. Moukalled & M. Darwish (2012) Transient Schemes for Capturing Interfaces of Free-Surface Flows, Numerical Heat Transfer, Part B: Fundamentals, 61:3, 171-203, DOI: 10.1080/10407790.2012.666145

To link to this article: http://dx.doi.org/10.1080/10407790.2012.666145

	Published online: 11 May 2012.
	Submit your article to this journal 🗷
hil	Article views: 190
a`	View related articles 🗗
4	Citing articles: 4 View citing articles 🗷

Full Terms & Conditions of access and use can be found at http://www.tandfonline.com/action/journalInformation?journalCode=unhb20

Copyright © Taylor & Francis Group, LLC ISSN: 1040-7790 print/1521-0626 online DOI: 10.1080/10407790.2012.666145



TRANSIENT SCHEMES FOR CAPTURING INTERFACES OF FREE-SURFACE FLOWS

F. Moukalled and M. Darwish

Mechanical Engineering Department, Faculty of Engineering & Architecture, American University of Beirut, Beirut, Lebanon

This article presents a new methodology for the development of Transient Interpolation for Capturing of Surfaces schemes suitable for the simulation of free-surface flows, which is given the acronym TICS. The newly developed approach is based on a switching strategy that combines a bounded high-order transient scheme with a bounded compressive transient scheme. Bounded high-order and compressive transient schemes are constructed by discretizing the transient term in the volume-of-fluid (r) equation over a temporal control-volume in a way similar to the discretization of the convection term over a spatial control-volume, allowing advances in building convective schemes to be exploited in the development of bounded high-order and compressive transient schemes. Following that approach, a bounded version of the second-order upwind Euler scheme is constructed (B-SOUE). The B-SOUE is used to develop a family of temporal compressive schemes that is denoted by the B-CE^m family, where "m" refers to the slope of the scheme on a temporal normalized variable diagram. The TICS methodology is then applied to the B-SOUE scheme and the B-CE^m family of schemes to create a new family of transient interface-capturing schemes that is designated by TICS^m. The virtues of the TICS^m family, in producing a steep interface for the volume-of-fluid (r) field that defines the volume fraction occupied by the different fluids in a computational domain, are demonstrated through results generated using two schemes of the family (TICS^{1.75} and TICS^{2.5}). The accuracy of the new transient TICS schemes is compared to the first-order Euler scheme, the Crank-Nicolson scheme, and the B-SOUE scheme by solving four pure advection test problems (advection of hollow shapes in an oblique flow field and advection of a solid body in a rotational flow field) and one flow problem (the break of a dam) using both the SMART and the STACS convective schemes. Results, displayed in the form of interface contours, demonstrate that predictions obtained with TICS^{1.75} and TICS^{2.5} are far more accurate and less diffusive, preserving interface sharpness and boundedness at all Courant number values considered.

INTRODUCTION

The growing need in a number of industries (e.g., automotive, chemical processing, aeronautic, etc.) for numerical simulation tools to help engineers tackle problems of continuously increasing complexity has been the major driver behind the

Received 10 November 2011; accepted 3 February 2012.

Financial support provided by the Lebanese National Council for Scientific Research (LNCSR) is gratefully acknowledged.

Address correspondence to F. Moukalled, Department of Mechanical Engineering, American University of Beirut, P.O. Box 11-0236, Riad El Soth, Beirut 1107 2020, Lebanon. E-mail: memouk@aub.edu.lb

NOMENCLATURE				
$ \begin{array}{c} \mathbf{B} \\ \mathbf{Co} \\ f(\theta) \end{array} $ $ \begin{array}{c} F(r) \\ m \\ n \\ P \\ r \\ \mathbf{S}_{f} \end{array} $	body force per unit volume Courant number blending function that varies between 0 and 1 advection term in <i>r</i> equation slope in <i>r</i> functional relationship total number of fluids pressure or main grid point volume fraction surface vector	θ $\mu, \mu^{(k)}$ $\rho, \rho^{(k)}$ τ ω Subscripts	angle between interface and velocity vector average and kth fluid dynamic viscosity average and kth fluid density shear stress tensor angular velocity s refers to compressive scheme	
t v V α	time velocity vector shared by all fluids cell volume parameter varying between 0 and 1	HR f Superscrip (k)	refers to high-resolution scheme refers to control-volume face pts refers to kth fluid	
Δt Δx , Δy	time step mesh size in x and y directions for Cartesian grid	$n \\ n-1 \\ n+1$	refers to current time step refers to previous time step refers to next time step	

sustained research effort in the area of computational fluid dynamics (CFD). Specifically the use of CFD in ship design and metal casting [1, 2] has put a renewed focus on the development of numerical techniques for the simulation of free-surface flows [3]. The proper simulation of these types of flows requires, among other things, a special set of transient and spatial schemes for the advection of sharp fluid—fluid interfaces.

In solving free-surface flow problems it is essential to preserve the sharpness of the interface between the two fluids. This has usually been achieved using two general methods denoted in the literature as *interface-tracking* methods and *interface-capturing* methods. In interface-tracking methods the interface is explicitly reconstructed and used in the evaluation of the advection scheme [4–12]. In interface-capturing methods, the interface is algebraically determined without reconstruction [13–23]. A powerful interface-capturing method is the volume-of-fluid (VOF) method [13–15]. In this method a scalar field (volume-of-fluid field, designated in this work by the r field) is introduced in the discretized governing equations to describe the volume fraction of a fluid in a cell. As such, information about interfaces is not readily available and is reconstructed when needed from the r field values.

It has been shown that in order to preserve the sharpness of interfaces, the discretization of the r equations in both the transient and spatial domains has to be accurate enough to prevent the smearing associated with numerical diffusion. In a recent article, Darwish and Moukalled [3] presented a new treatment for spatial schemes within the context of the VOF method [13–15].

Little work has been done on devising transient schemes suitable for predicting free-surface flows, and usually the Euler [24], the Crank-Nicolson [25], or the second-order upwind Euler [26] scheme has been used. The numerical diffusion produced by the first-order Euler scheme [24] is akin to that of the first-order-upwind scheme used in spatial discretization and thus should be avoided in order to preserve the sharpness of the interface. On the other hand, while the second-order

Crank-Nicolson and the second-order upwind Euler schemes are less diffusive their degree of success is highly dependent on the value of the Courant number.

In this article, a new approach for developing finite-volume-based transient schemes for the discretization of the r field, denoted by TICS (Transient Interpolation for Capturing of Surfaces), is developed. The new methodology exploits for its formulation the similarity between advection discretization in space and transient discretization in time. The new methodology is used to construct two new schemes that are compared in terms of accuracy to the Euler scheme, the well-known crank-Nicolson [25] scheme, and to a newly developed bounded version of the second-order upwind Euler scheme; and it is shown to be superior in producing lower numerical diffusion while preserving interface sharpness and boundedness.

In the remainder of this article, after a brief description of the VOF method, applying the finite-volume principles to the transient discretization approach is described. This is followed by a demonstration of the similarity between transient and spatial schemes. Then a number of transient schemes are reformulated following the finite-volume approach and the new TICS approach is detailed. Finally, results related to the advection of three hollow shapes in an oblique velocity field and a slotted circle in a rotational flow field in addition to the well-known dam-break problem are presented and discussed. Predictions are obtained using the upwind [27], Crank-Nicolson [25], bounded second-order upwind Euler, and the two new TICS-based transient schemes with either the SMART [28, 29] or the STACS [3] convective scheme.

THE VOLUME-OF-FLUID METHOD

The volume-of-fluid method [13], depicted schematically in Figure 1a, is a surface-capturing method for predicting flows composed of multiple immiscible fluids. The various fluids are assumed to share a common velocity field, and solutions are obtained by solving the averaged Navier-Stokes equations given by

$$\frac{\partial(\rho)}{\partial t} + \nabla \cdot (\rho \mathbf{v}) = 0$$

$$\frac{\partial(\rho \mathbf{v})}{\partial t} + \nabla \cdot (\rho \mathbf{v} \mathbf{v}) = \nabla \cdot \tau - \nabla P + \mathbf{B}$$
(1)

with density and viscosity evaluated using the following mixture relations:

$$\rho = \sum_{k=1}^{n} r^{(k)} \rho^{(k)} \quad \text{and} \quad \mu = \sum_{k=1}^{n} r^{(k)} \mu^{(k)} \quad n = \text{number of fluids}$$
 (2)

where $r^{(k)}$ represents the volume fraction of the kth fluid. These $r^{(k)}$ fields are computed by solving scalar convection equations defined as

$$\frac{\partial r^{(k)}}{\partial t} + \mathbf{v} \cdot \nabla r^{(k)} = 0 \quad \text{for } k = 1, 2, \dots, (n-1) \quad n = \text{number of fluids}$$
 (3)

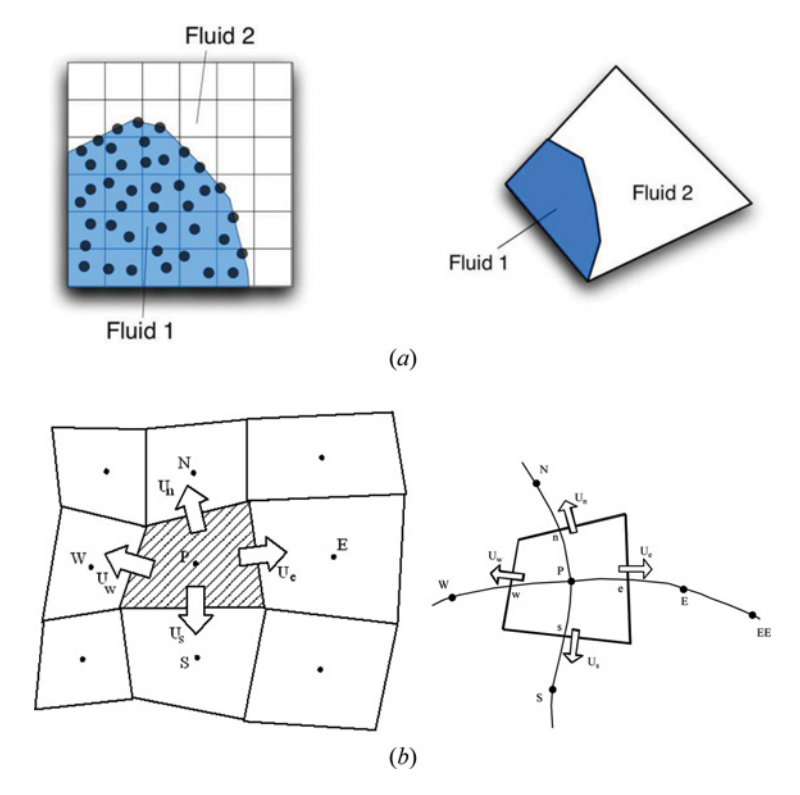


Figure 1. (a) Schematic of the volume-of-fluid method. (b) Discretization of the physical domain into spatial control-volumes (color figure available online).

and constrained by a conservation-of-volume equation given by

$$\sum_{k=1}^{n} r^{(k)} = 1 \quad \text{for } k = 1, 2, \dots, n \quad n = \text{number of fluids}$$
 (4)

For the case of incompressible fluids, the continuity equation can be simplified to

$$\nabla \cdot \mathbf{v} = 0 \tag{5}$$

It is this form of the continuity equation [Eq. (5)] that is used in the derivation of the pressure-correction equation in order to avoid numerical difficulties that arise when large disparities in fluid densities exist.

FINITE-VOLUME DISCRETIZATION OF THE TRANSIENT TERM IN THE $\it r$ FIELD EQUATION

In the finite-volume method [30–44], solutions are obtained by subdividing the physical domain under consideration into a finite number of control-volumes, where

each is associated with a grid point placed at its geometric center (Figure 1b). The partial differential equations mathematically describing the conservation laws [e.g., Eqs. (1) and (3)] are integrated over each control-volume, and profile approximations for the diffusion and convection terms are made in each coordinate direction to replace the derivatives with algebraic expressions. The integral value of the source term (and usually the transient term) over a control-volume is normally evaluated by assuming the source at the control-volume center to be equal to the mean value over the whole control-volume. The resulting system of algebraic equations is then solved using a line-by-line tridiagonal matrix algorithm [27] to obtain the solution.

For unsteady problems, the r field equation [Eq. (3)] may generally be written as

$$\frac{\partial r}{\partial t} = F(r) \tag{6}$$

in which the superscript (k) is dropped for convenience and F(r) represents the advection term. The usual practice followed in the transient discretization of Eq. (6) is to integrate both sides of the equation over the time interval $[t, t+\Delta t]$ to yield

$$\int_{t}^{t+\Delta t} \frac{\partial r}{\partial t} dt = \int_{t}^{t+\Delta t} F(r) dt = [\text{temporal average of } F(r)] \Delta t$$
 (7)

Then, the discretized form is obtained as

$$r^{t+\Delta t} = r^t + \overline{F(r)} \ \Delta t \tag{8}$$

This formulation yields exact integral value of the term $(\partial r/\partial t)$, however, the value of $\overline{F(r)}$ is highly dependent on the scheme used. In general, $\overline{F(r)}$ is written as

$$\overline{F(r)} = \alpha F(r^t) + (1 - \alpha) F(r^{t + \Delta t})$$
(9)

Different schemes are obtained depending on the value of α . Specifically, the explicit Euler, fully implicit Euler, and Crank-Nicolson schemes are obtained by setting α to 1, 0, and 1/2, respectively. The only unconditionally stable discretization [27] is the one obtained using the fully implicit scheme, which is first-order-accurate, highly diffusive, and consequently not suitable as an interface-capturing-scheme. Even though the Crank-Nicolson scheme is second-order-accurate, it suffers from oscillation at values of Courant number greater than 2 in one-dimensional space.

A better approach, followed in this work, is to apply the finite-volume principles to the transient discretization. For that purpose, similar to the spatial discretization of the convective term, time integration is performed over a temporal control-volume, as shown in Figure 2a. Unlike the previous method, integration of Eq. (5) is performed over the time period $[t - \Delta t/2, t + \Delta t/2]$, yielding

$$\int_{t-\Delta t/2}^{t+\Delta t/2} \frac{\partial r}{\partial t} dt = \int_{t-\Delta t/2}^{t+\Delta t/2} F(r) dt$$
 (10)

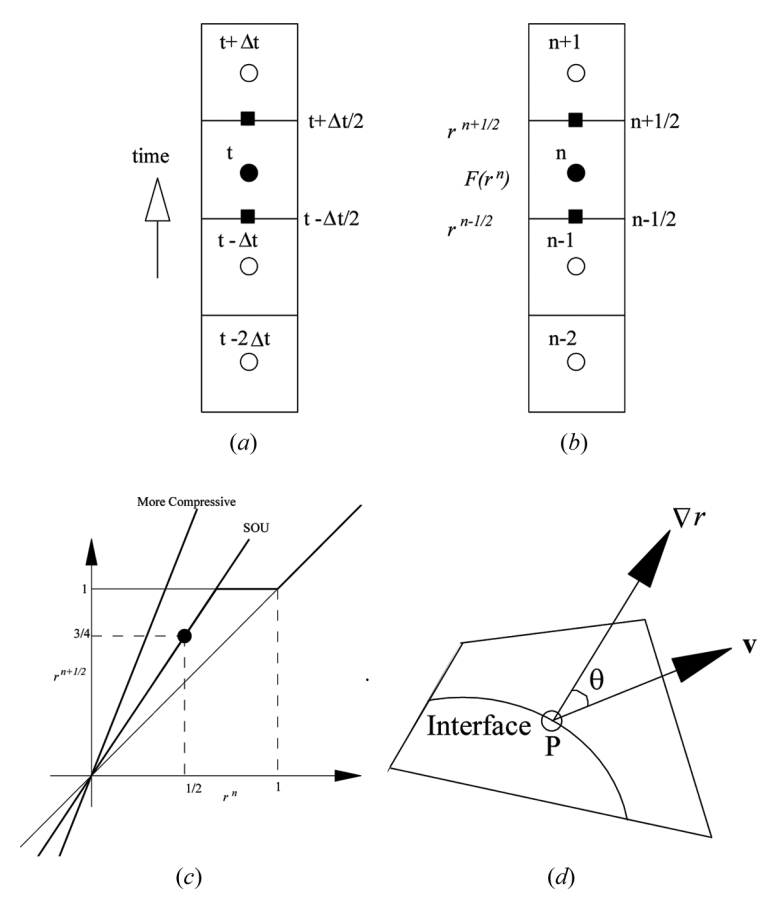


Figure 2. (a) Temporal control-volumes. (b) Normalized variables diagram of compressive transient schemes. (c) Angle between interface and velocity vector at the center of a spatial control-volume.

The discretized form of Eq. (10) may be written as

$$r^{t+\Delta t/2} = r^{t-\Delta t/2} + \overline{F(r)} \, \Delta t \tag{11}$$

or, equivalently as

$$r^{n+1/2} = r^{n-1/2} + \overline{F(r)} \, \Delta t$$
 (12)

It is worth noting that the source term $\overline{F(r)}$ evaluated implicitly at time t (i.e., $\overline{F(r)} = F(r^n)$ with $\alpha = 0$) is second-order-accurate over the interval $[t - \Delta t/2, t + \Delta t/2]$. The onus of the discretization is now moved to the transient term on the left-hand side (i.e., the term $\partial r/\partial t$). The resemblance of the transient term to the advection term can be used advantageously to develop new transient schemes. In what follows several known transient schemes are reconstructed following the reasoning used to develop advection schemes in setting the ground for the

development of the newly suggested transient scheme in the context of a temporal control-volume.

First-Order Transient Euler Schemes

The transient first-order implicit Euler scheme is obtained by using a first-order transient "upwind" interpolation profile. That is, the value of r at the temporal control-volume face is set equal to the value at the upwind control-volume center.

$$r^{n+1/2} = r^n$$
 and $r^{n-1/2} = r^{n-1}$ (13)

Using Eq. (13), Eq. (12) becomes

$$\frac{r^n - r^{n-1}}{\Lambda t} = F(r^n) \tag{14}$$

which is the first-order implicit Euler scheme.

The transient first-order explicit Euler scheme is obtained by using a first-order transient "downwind" interpolation profile. That is, the value of r at the temporal control-volume face is set equal to the value at the downwind control-volume center.

$$r^{n+1/2} = r^{n+1}$$
 and $r^{n-1/2} = r^n$ (15)

Using Eq. (15), Eq. (12) becomes

$$\frac{r^{n+1} - r^n}{\Delta t} = F(r^n) \tag{16}$$

which is the first-order explicit Euler scheme.

Second-Order Central Scheme (Crank-Nicolson)

The Crank-Nicolson (CN) scheme is obtained by calculating the value of r at an interface as the average of the r values at the main points straddling the interface, i.e.,

$$r^{n+1/2} = \frac{1}{2}r^{n+1} + \frac{1}{2}r^n$$
 and $r^{n-1/2} = \frac{1}{2}r^n + \frac{1}{2}r^{n-1}$ (17)

Substituting in Eq. (12), the discretized r field equation is obtained as

$$\frac{r^{n+1} - r^{n-1}}{2 \Delta t} = F(r^n) \tag{18}$$

As shown below, the Crank-Nicolson scheme can also be obtained as the sum of the upwind and downwind transient schemes.

Upwind
$$\rightarrow \frac{r^n - r^{n-1}}{\Delta t} = F(r^n)$$
 (19)

Downwind
$$\rightarrow \frac{r^{n+1} - r^n}{\Delta t} = F(r^n)$$
 (20)

Upwind + downwind
$$\rightarrow \frac{r^n - r^{n-1}}{\Delta t} + \frac{r^{n+1} - r^n}{\Delta t} = F(r^n) + F(r^n)$$

$$\rightarrow \frac{r^{n+1} - r^{n-1}}{2 \Delta t} = F(r^n)$$

$$\rightarrow \text{Crank - Nicolson}$$
(21)

This formulation enables the implementation of the Crank-Nicolson scheme within an implicit scheme framework as a two-step procedure. In the first step, an implicit Euler formulation is used to find r^n from

$$r^n = r^{n-1} + \Delta t \ F(r^n) \tag{22}$$

while in the second step the Crank-Nicolson value at time n + 1 is found explicitly as

$$\frac{r^{n+1} - r^n}{\Delta t} = F(r^n) = \frac{r^n - r^{n-1}}{\Delta t} \Rightarrow r^{n+1} = 2r^n - r^{n-1}$$
 (23)

In terms of implementation, to find the solution at time $t + \Delta t$, the time step for the Crank-Nicolson scheme is chosen to be half Δt , i.e., $\Delta t_{\text{Crank-Nicolson}} = \Delta t/2$. In this work, the Crank-Nicolson scheme is implemented using the two-step procedure described above.

Second-Order Upwind Euler (SOUE) Scheme

Using a second-order "upwind" interpolation profile [26], the interface r values are approximated as

$$r^{n+1/2} = \frac{3}{2}r^n - \frac{1}{2}r^{n-1}$$
 and $r^{n-1/2} = \frac{3}{2}r^{n-1} - \frac{1}{2}r^{n-2}$ (24)

Substituting in Eq. (12), the discretized r field equation is obtained as

$$\frac{3r^n - 4r^{n-1} + r^{n-2}}{2 \Delta t} = F(r^n) \tag{25}$$

which is the second-order upwind Euler (SOUE) scheme.

Bounded Second-Order Upwind Euler (B-SOUE) Scheme

The second-order transient "upwind" interpolation, like its spatial counterpart, is not a bounded scheme in that it can yield values for r that are above or below the local maximum or minimum, respectively. In the volume fraction equation this would lead to unacceptable values above 1 or below 0. To resolve this problem a bounded version of the scheme is used in order for r^n to be in the range 0 to 1.

The implementation of the bounding is similar to that of the convection boundedness criterion (CBC) [29]. Mathematically, the bounded second-order upwind Euler (B-SOUE) scheme is given by

$$r^{n+1/2} = \operatorname{Max} \left[\operatorname{Min} \left(\frac{3}{2} r^n - \frac{1}{2} r^{n-1}, 1 \right), 0 \right] \text{ and}$$

$$r^{n-1/2} = \operatorname{Max} \left[\operatorname{Min} \left(\frac{3}{2} r^{n-1} - \frac{1}{2} r^{n-2}, 1 \right), 0 \right]$$
(26)

Note that the values for $r^{n-1/2}$ are already bounded between (0, 1).

It is important to mention here that implicit bounding of the Crank-Nicolson scheme is not achievable, as its implementation involves an explicit step [Eq. (23)]. Definitely, explicit bounding of Eq. (23) is possible; however, it causes nonconservation of the r field as time progresses (i.e., due to explicit clipping of the r values, the total initial value of r is not conserved). For this reason, attention in this work is focused on conservative implicit bounding.

Compressive Euler Schemes

For interface capturing, a compressive transient scheme is required [3], which can be built in a way similar to spatial compressive schemes. Considering the normalized variable diagram (NVD) [45] of the second-order upwind Euler (SOUE) scheme [46] shown in Figure 2b, a more compressive scheme can be developed by using a steeper slope than for the SOUE scheme and bounding the resulting value between 0 and 1. Mathematically, this is equivalent to having a base scheme of

$$r^{n+1/2} = mr^n - (m-1)r^{n-1}$$
 and $r^{n-1/2} = mr^{n-1} - (m-1)r^{n-2}$ (27)

Moreover, it is to be noted that for the SOUE scheme, m = 3/2; taking a value for m > 3/2 yields a more compressive scheme, but the accuracy decreases to first-order.

The equivalent bounded form of Eq. (27) becomes

$$r^{n+1/2} = \operatorname{Max} \left\{ \operatorname{Min} \left[mr^{n} - (m-1)r^{n-1}, 1 \right], 0 \right\}$$

$$r^{n-1/2} = \operatorname{Max} \left\{ \operatorname{Min} \left[mr^{n-1} - (m-1)r^{n-2}, 1 \right], 0 \right\}$$
(28)

The resulting family of schemes whose functional relationships are given by Eq. (28) is denoted in this work by B-CE^m, where "m" changes depending on the value used. The implementation of the above scheme is done via the deferred correction procedure [28], whereby the discretization of $r^{n+1/2}$ is written as

$$r^{n+1/2} = r^{n} + \left(\operatorname{Max} \left\{ \operatorname{Min} \left[mr^{n} - (m-1)r^{n-1}, 1 \right], 0 \right\} - r^{n} \right)$$

$$r^{n-1/2} = \operatorname{Max} \left\{ \operatorname{Min} \left[mr^{n-1} - (m-1)r^{n-2}, 1 \right], 0 \right\}$$
(29)

where r^n is evaluated implicitly at the current iteration while other terms are evaluated explicitly using values from the previous time steps and/or previous iteration.

Transient Interpolation for Capturing of Surfaces (TICS)

In [3] it was shown that the best approach for developing an advection interface-capturing scheme is through a switching strategy [17, 48], whereby the values of a compressive and a high-resolution (i.e., a bounded high-order) advection scheme are blended together, with the blending factor depending on the angle between the flow direction and the grid lines. In the context of a transient finite-volume discretization, a similar argument is projected to hold for the transient term. Therefore, a transient scheme for capturing interfaces of free-surface flows should be based on a combination of a compressive (C) and a high-resolution (HR) transient scheme, with the blending parameter being function of the angle θ between the interface direction and the velocity vector. The angle can be determined at the spatial control-volume center using the velocity vector and the gradient of the r field, whose unit vector represents the direction normal to the interface (see Figure 3b). Mathematically, θ is calculated as

$$\cos(\theta) = \left| \frac{\nabla r \cdot \mathbf{v}}{\|\nabla r\| \|\mathbf{v}\|} \right| \tag{30}$$

With TICS the value of r at a temporal control-volume face is given by

$$r^{n+1/2} = r_{\theta}^{n+1/2} = r_{C}^{n+1/2} f(\theta) + r_{HR}^{n+1/2} [1 - f(\theta)]$$

$$r^{n-1/2} = r_{\theta}^{n-1/2} = r_{C}^{n-1/2} f(\theta) + r_{HR}^{n-1/2} [1 - f(\theta)]$$
(31)

In Eq. (31), $f(\theta)$ is a blending function that varies between 0 and 1.

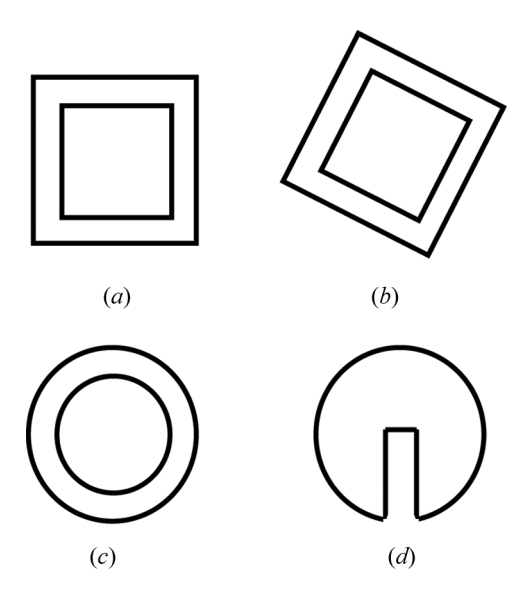


Figure 3. Schematics of the advected (a) hollow square, (b) rotated hollow square, (c) hollow circle, and (d) slotted circle problems.

In the newly suggested TICS methodology, the HR scheme selected is the bounded second-order Upwind Euler scheme, while the compressive scheme is the previously presented bounded compressive Euler scheme. Moreover, in order to minimize the stepping behavior of the compressive Euler scheme, the blending between the two schemes is performed using Eq. (31) with $f(\theta)$ set to $[\cos(\theta)]^4$, which enables a rapid but smooth switching away from the compressive scheme. The family of schemes that can be developed following the TICS approach, based on the previously presented compressive Euler and bounded second-order Euler schemes, is denoted as the TICS^m family of schemes. It should be obvious that the TICS strategy is not limited to the above schemes and can be used to devise a family of free-surface transient schemes by using different combinations of C/HR transient schemes.

The functional relationship for the TICS^m family of schemes is given by

$$\begin{split} r_{TICS}^{n+1/2} &= \mathrm{Max} \big\{ \mathrm{Min} \big[m r^n - (m-1) r^{n-1}, \ 1 \big], \ 0 \big\} [\cos(\theta)]^4 + \\ &\qquad \qquad \mathrm{Max} \bigg[\mathrm{Min} \Big(\frac{3}{2} r^n - \frac{1}{2} r^{n-1}, \ 1 \Big), 0 \Big] \Big\{ 1 - [\cos(\theta)]^4 \Big\} \\ r_{TICS}^{n-1/2} &= \mathrm{Max} \big\{ \mathrm{Min} \big[m r^{n-1} - (m-1) r^{n-2}, \ 1 \big], \ 0 \big\} [\cos(\theta)]^4 + \\ &\qquad \qquad \mathrm{Max} \bigg[\mathrm{Min} \Big(\frac{3}{2} r^{n-1} - \frac{1}{2} r^{n-2}, \ 1 \Big), \ 0 \Big] \Big\{ 1 - [\cos(\theta)]^4 \Big\} \end{split}$$

In this work the TICS methodology is used to develop and test two new schemes, denoted by TICS^{1.75} and TICS^{2.5}, which are obtained by assigning m the values of 1.75 and 2.5, respectively.

RESULTS AND DISCUSSION

In this section, the performance of the newly developed transient interface-capturing schemes $TICS^{1.75}$ and $TICS^{2.5}$ in solving four advection test problems (Figures 3a-3d) and one flow problem is compared to that of the first-order Euler, the bounded second-order Euler, and the Crank-Nicolson transient schemes. Results generated using both the SMART and STACS convective schemes are reported in the form of r-contour plots for three values of Courant number (Co), defined at a control-volume face as

$$Co_f = \frac{\mathbf{v}_f \cdot \mathbf{S}_f \ \Delta t}{V_f} \tag{33}$$

Moreover, all calculations were performed assuming that surface-tension effects are negligible.

Advection of Hollow Shapes in an Oblique Velocity Field

Three different hollow shapes [49, 50] are convected in an oblique velocity field defined by v[2, 1]. The computational domain is a square with sides of length 1 m, subdivided into 200×200 (40,000) square control-volumes. The following three shapes, depicted in Figures 3a-3c, are considered: a hollow square (Figure 3a)

aligned with the coordinate axes of the outer and inner sides with values of $0.3 \,\mathrm{m}$ and $0.2 \,\mathrm{m}$, respectively; a hollow square rotated through an angle of 26.57° with respect to the x axis (Figure 3b) of dimensions similar to those of the above hollow square; and a hollow circle (Figure 3c) with outer and inner diameters with values of $0.3 \,\mathrm{m}$ and $0.2 \,\mathrm{m}$, respectively.

All shapes are initially centered at (0.2, 0.2) m, with their exact positions centered at (0.8, 0.5) m after 0.3 s. Computations using the various schemes were performed for three different time steps, $\Delta t = 6.25 \times 10^{-4}$ s, 1.25×10^{-3} s, and 2.5×10^{-3} s, yielding Courant number values of 0.25, 0.5, and 1, respectively. Computations at any time step were terminated when the maximum absolute residual dropped below a very small number ε_s , which was set at 5×10^{-5} . The exact solutions for the problems considered are presented in Figures 3a-3c. In all calculations, the densities of the fluid and convected shape are equal.

Results for the various shapes are depicted in Figures 4–9. The SMART convective scheme results are displayed in Figures 4, 6, and 8, while the STACS scheme results are shown in Figures 5, 7, and 9. For both convective schemes, the *r* fields obtained using the various transient schemes at different Co values after the lapse of 0.3 s are presented. As depicted, the trend is the same for all shapes. The SMART scheme profiles (Figures 4, 6, and 8) obtained using the various transient schemes are more diffusive than the corresponding profiles generated using the STACS convective scheme (Figures 5, 7, and 9), for reasons detailed by Darwish and Moukalled [3]. The first-order Euler scheme profiles obtained with SMART (Figures 4*a*, 6*a*, and 8*a* are highly diffusive at all Co value considered, with false diffusion effects increasing as the Co value increases. This is expected, as numerical diffusion resulting from temporal discretization of the implicit Euler scheme is directly proportional to the Co value [3, 51].

Euler profiles generated using STACS are less diffusive but are associated with the formation of wiggles along interfaces normal to the flow direction. The amplitude of these wiggles increases as Co increases (Figures 5a, 7a, and 9a). Profiles generated with the second-order Crank-Nicolson scheme (Figures 4b–9b) are much less diffusive than the Euler (upwind) profiles, and at low Co are of quality equivalent to, if not better than the ones obtained with the B-SOUE scheme. The CN profiles obtained with STACS (Figures 4b, 6b, and 8b) are sharper than those obtained with SMART (Figures 5b, 7b, and 9b). The major problem with the CN scheme, however, is its boundedness at higher values of Co. As depicted in Figures 4b-9b, unphysical values of r, below 0 and above 1, are obtained for $Co \ge 0.5$, with the range of values becoming larger as Co increases. This limits the usefulness of the CN to low Co values, which is a major constraint. Results obtained with the B-SOUE scheme (Figures 4c-9c) are slightly more diffusive than the ones obtained with the CN scheme; however, the r values are all bounded in the range between 0 and 1. With the SMART convective scheme, the B-SOUE (Figures 4c, 6c, and 8c) transient scheme is not capable of sharply resolving the interfaces. Similar to the CN scheme, sharper interfaces are obtained with the B-SOUE scheme when using STACS (Figures 5c, 7c, and 9c) in comparison with those obtained with the SMART convective scheme (Figures 4c, 6c, and 8c). With the STACS convective scheme, however, wiggles along the interfaces in the direction of the flow are generated at Co = 1 for the rotated hollow square and hollow circle problems. Interfaces predicted by the newly developed TICS^{1.75} (Figures 4d–9d) and TICS^{2.5} (Figures 4e–9e) transient

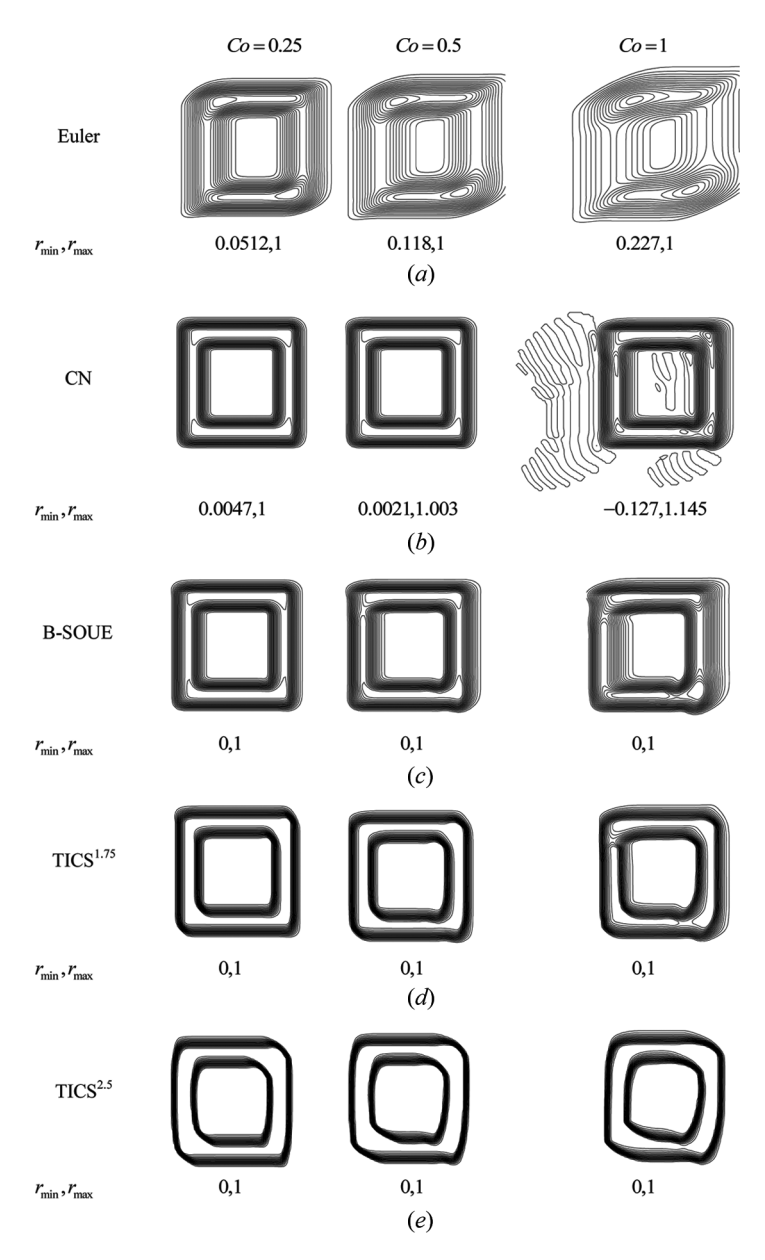


Figure 4. Contour plots of the r field for the advection in an oblique flow field of the hollow square problem computed using the SMART advection scheme.

schemes are sharper than those produced by the previously predicted schemes, with profiles generated by TICS^{2,5} being the sharpest. This is a clear indication of the superiority of the TICS approach.

When using the STACS convective scheme, similar to results obtained with the B-SOUE scheme, profiles for the rotated hollow square and hollow circle problems

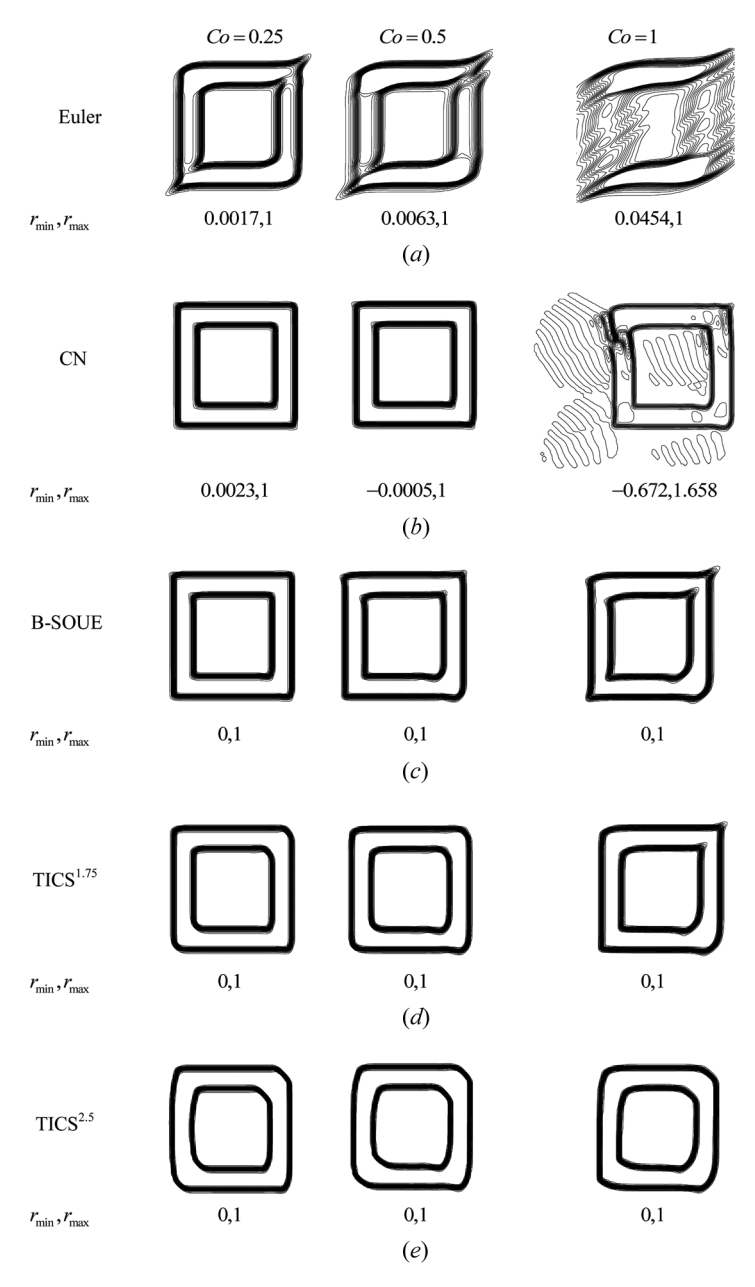


Figure 5. Contour plots of the r field for the advection in an oblique flow field of the hollow square problem computed using the STACS advection scheme.

predicted by $TICS^{1.75}$, even though sharp, show wiggles along interfaces in the direction of the flow at Co=1. The amplitude of these wiggles is lower than the ones obtained with the B-SOUE transient scheme. On the other hand, profiles obtained with $TIC^{2.5}$ are free of wiggles.

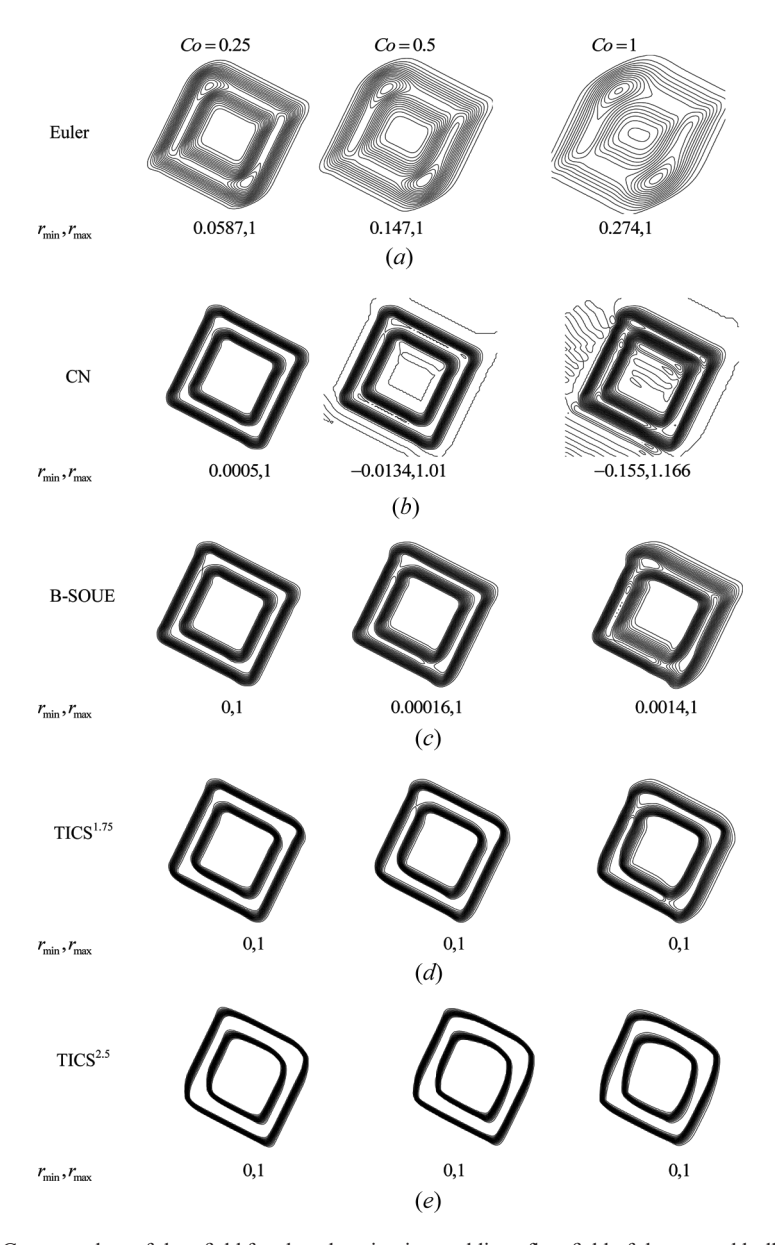


Figure 6. Contour plots of the r field for the advection in an oblique flow field of the rotated hollow square problem computed using the SMART advection scheme.

To understand the cause of these wiggles, additional computations for the rotated hollow square and hollow circle problems were performed; the results are displayed in Figures 10 and 11, respectively. Contours presented in Figure 10 are computed for Co values of 1.5, 2, and 2.67. Contours predicted by the B-SOUE scheme and displayed in Figure 10a show wiggles along interfaces normal to the flow direction. The amplitude of these wiggles increases as the Co value increases. As

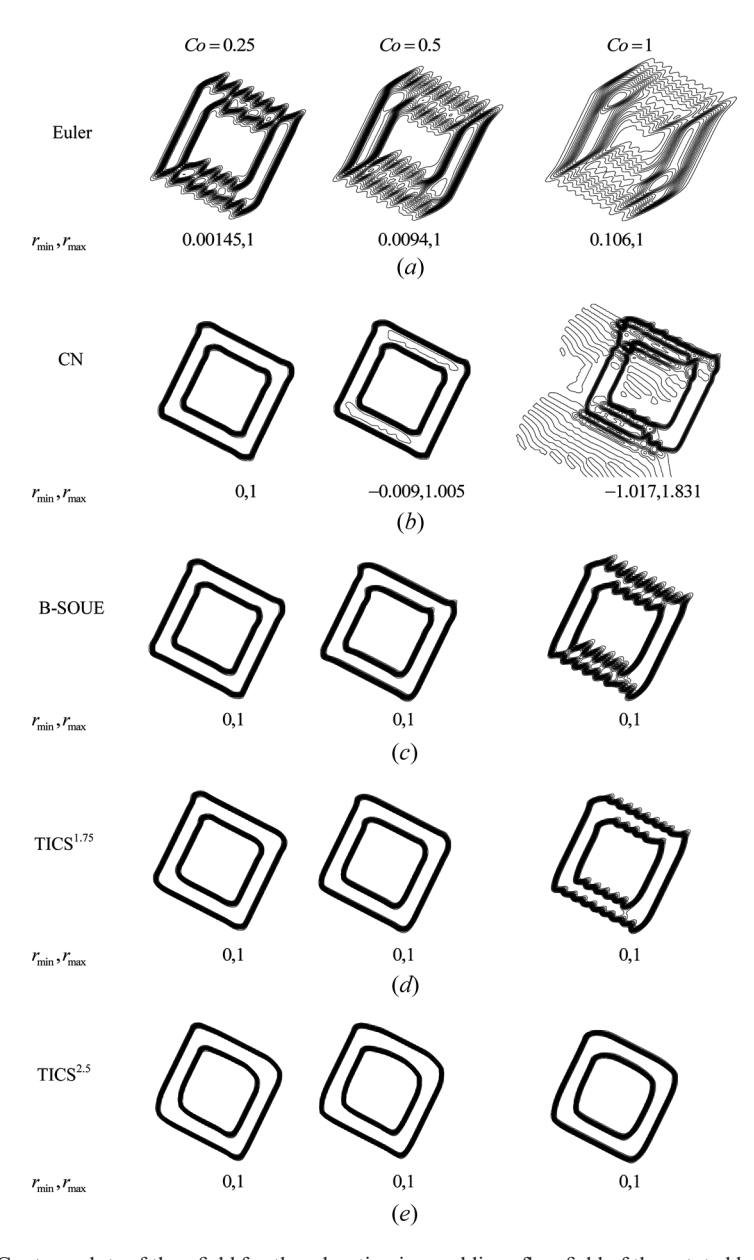


Figure 7. Contour plots of the r field for the advection in an oblique flow field of the rotated hollow square problem computed using the STACS advection scheme.

shown in Figure 10b, the use of the TICS^{1.75} scheme reduces the amplitude of these wiggles but does not eliminate them. The value of slope m in TICS^{1.75} is only 0.25 higher than the value of m in the B-SOUE, which indicates that the scheme is still diffusive. However, the use of the TIC^{2.5} greatly improves results, with the wiggles almost nonexistent at Co = 1.5, barely apparent at Co = 2, and of low amplitude

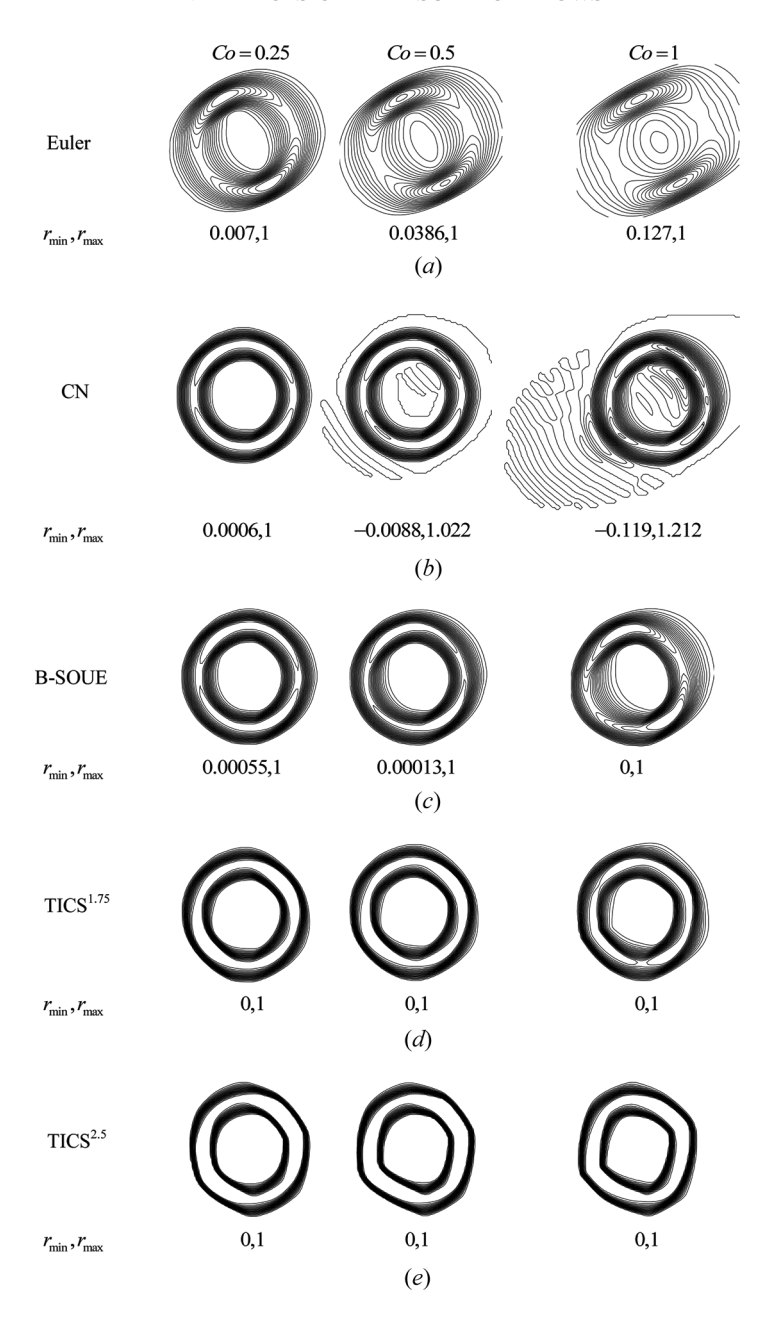


Figure 8. Contour plots of the r field for the advection in an oblique flow field of the hollow circle problem computed using the SMART advection scheme.

at the highest Co considered (Co = 2.67). To check continuation of the trend as m increases, a value of 3 was assigned to m and results were generated using a third scheme (TICS³). Contours generated with TICS³ are displayed in Figure 10d. As

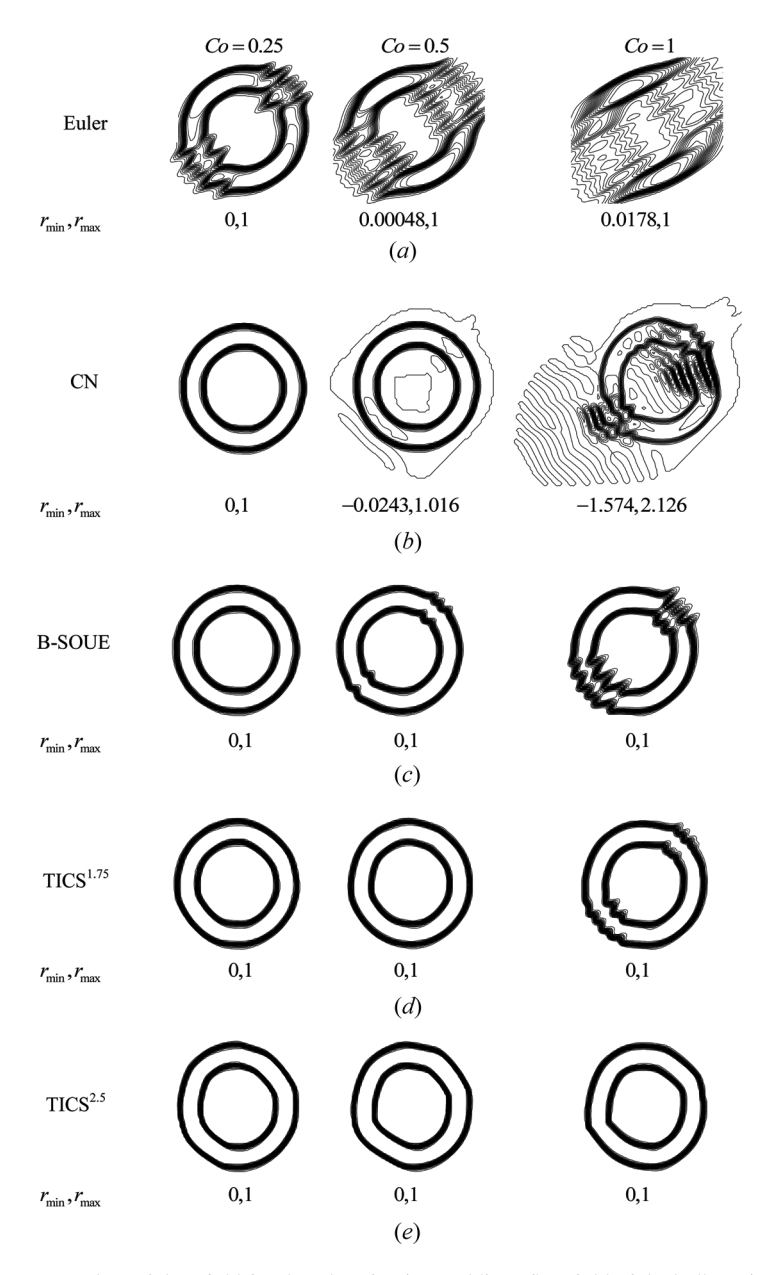


Figure 9. Contour plots of the r field for the advection in an oblique flow field of the hollow circle problem computed using the STACS advection scheme.

shown, wiggles at interfaces are almost nonexistent at all Co values considered. This is a clear demonstration that the use of a compressive transient scheme reduces the amplitude of wiggles and, depending on the Co values considered, may completely eliminate them. The results presented, and others not presented for compactness, indicate that wiggles appear only with STACS. No wiggles were generated when

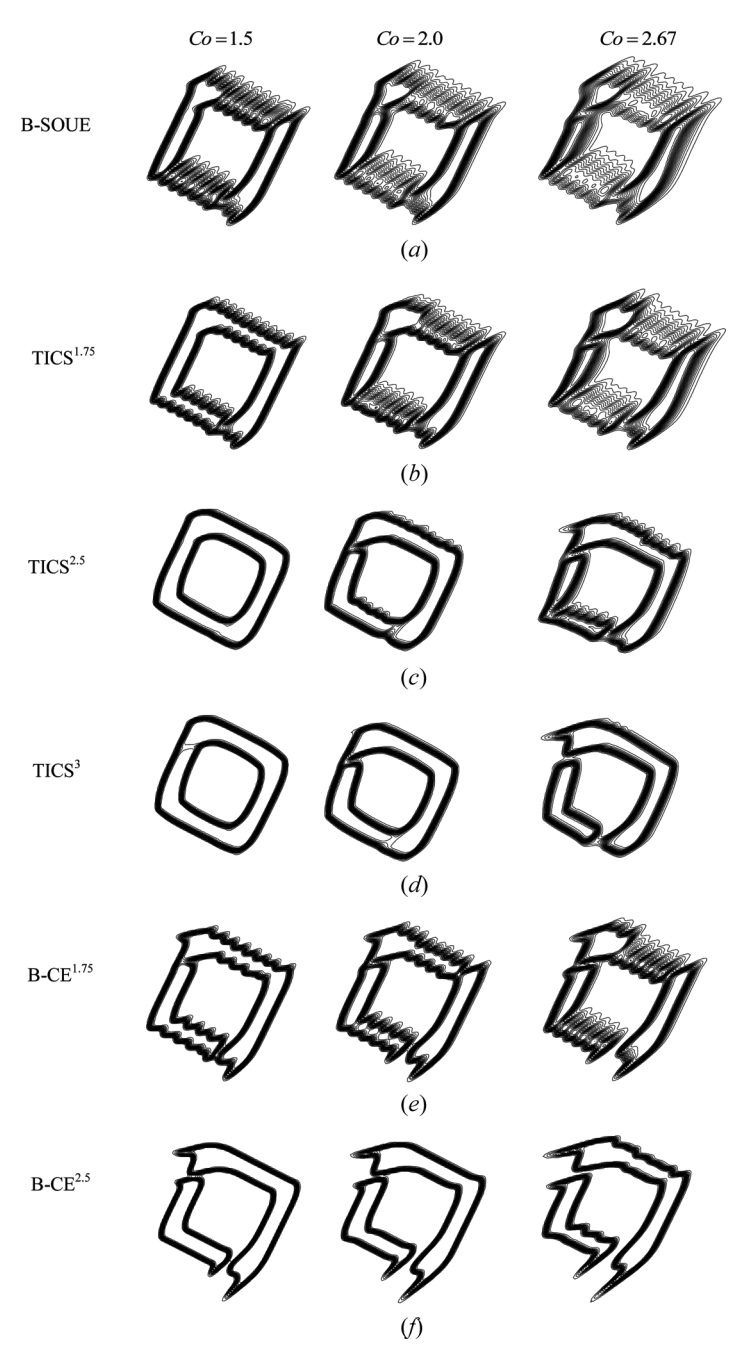


Figure 10. Comparison of the *r*-contour plots computed using the STACS advection scheme and a variety of transient schemes at high Co values for the advection in an oblique flow field of the rotated hollow square problem.

using the SMART convective scheme. Based on this, it can safely be stated that wiggles appear due to the dispersive effect of the convective STACS scheme, which switches to the highly compressive SUPERBEE scheme [52] when the normal to the interface is in the direction of the flow [3] and are eliminated (minimized) with the use of a transient compressive scheme.

The drawback of using a highly compressive transient scheme, however, is the clipping problem that deteriorates the convected shape (e.g., Figure 10d at Co = 2.67). To further investigate this issue, computations were performed using a purely compressive transient scheme; results are depicted in Figures 10e and 10f. Contours of the r-field shown in Figure 10e, obtained using the B-CE^{1.75} scheme, are close to those predicted by the B-SOUE scheme. This is expected, for the reasons mentioned earlier. The difference between the two results is a reduction in the amplitude of wiggles and the splitting of the convected profile. This issue is further revealed by plots displayed in Figure 10f where the wiggles are almost nonexistent and shape splitting occurs at all Co values.

To demonstrate the need for TICS, contours of the convected hollow circle problem obtained with TICS and compressive schemes for Co = 0.5, 1, and 1.5 are displayed in Figure 11. Whereas profiles generated with TICS^{1.75} (Figure 11*a*) and

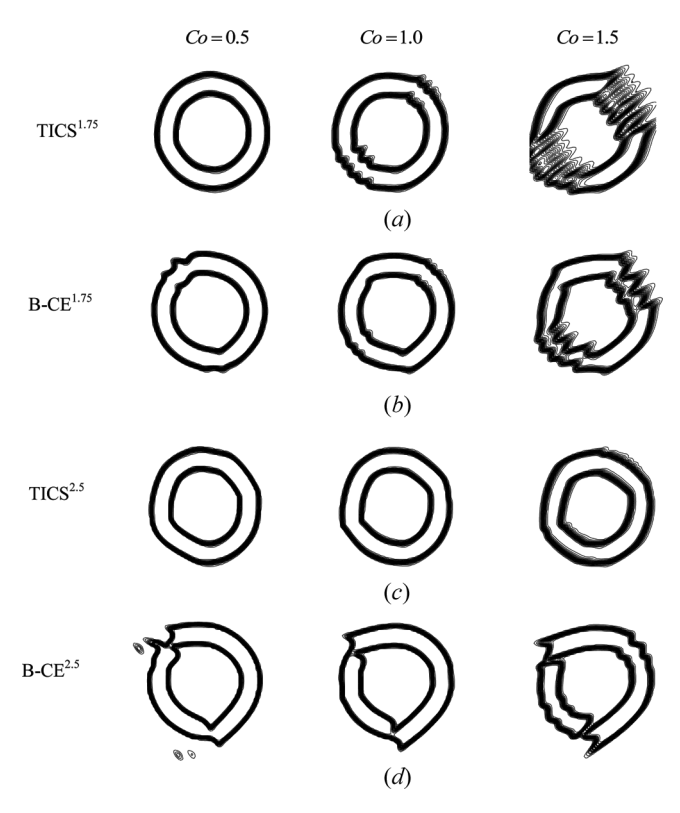


Figure 11. Comparison of the *r*-contour plots computed using the STACS advection scheme and either a TICS or a bounded compressive transient scheme for the advection in an oblique flow field of the hollow circle problem.

B_CE^{1.75} (Figure 11*b*) are of comparable quality, those obtained with TICS^{2.5} (Figure 11*c*) and B_CE^{2.5} (Figure 11*d*) are very different. The highly compressive B-CE^{2.5} scheme causes splitting of the convected shape, as shown in Figure 11*d*. On the other hand, results shown in Figure 11*c* generated by TICS^{2.5} are very smooth and sharply resolves the interfaces. This is a clear indication of the need for the TICS

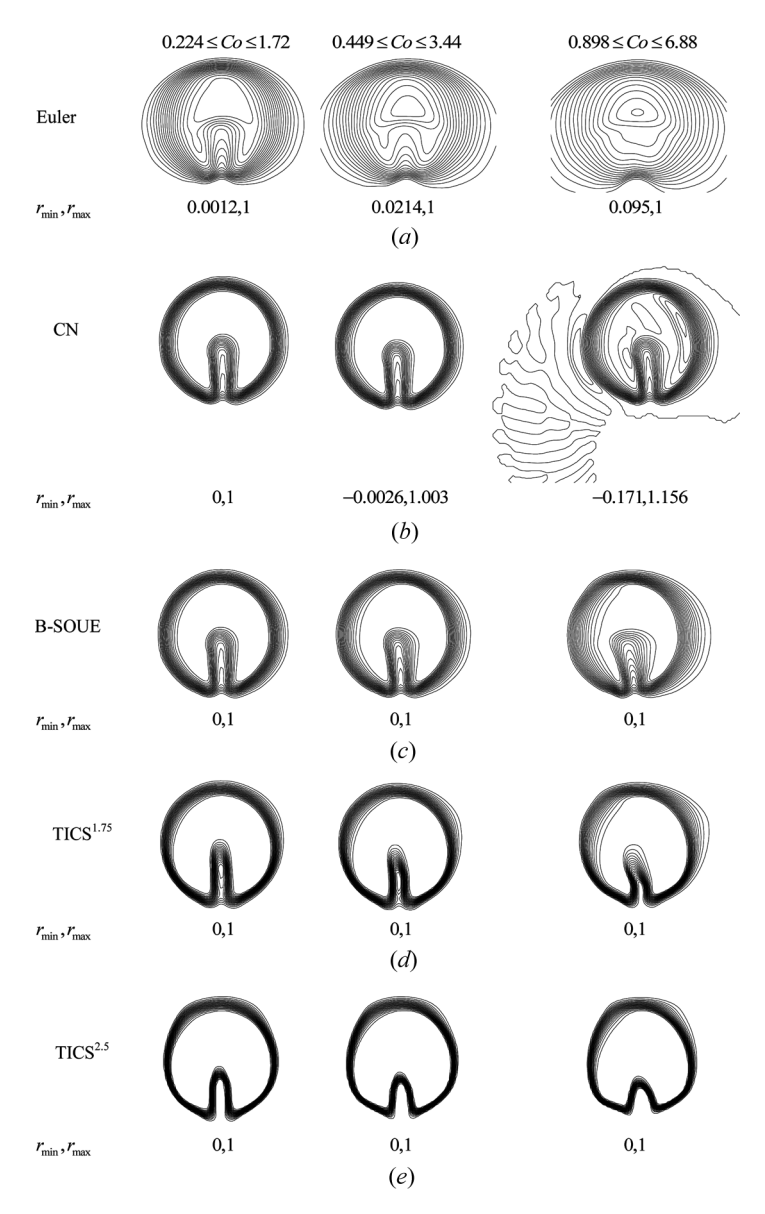


Figure 12. Contour plots of the r field at high Co values for the advection in an oblique flow field of the hollow circle problem computed using the STACS advection scheme.

approach to develop schemes that are capable of switching from a compressive to a high-resolution mode or to a combination of the two when needed.

By comparing contours obtained with the various schemes (Figures 4–11), it is clear that the performance of TICS^{2.5} is superior to all other schemes, preserving sharp interfaces without noticeably altering the convected shapes.

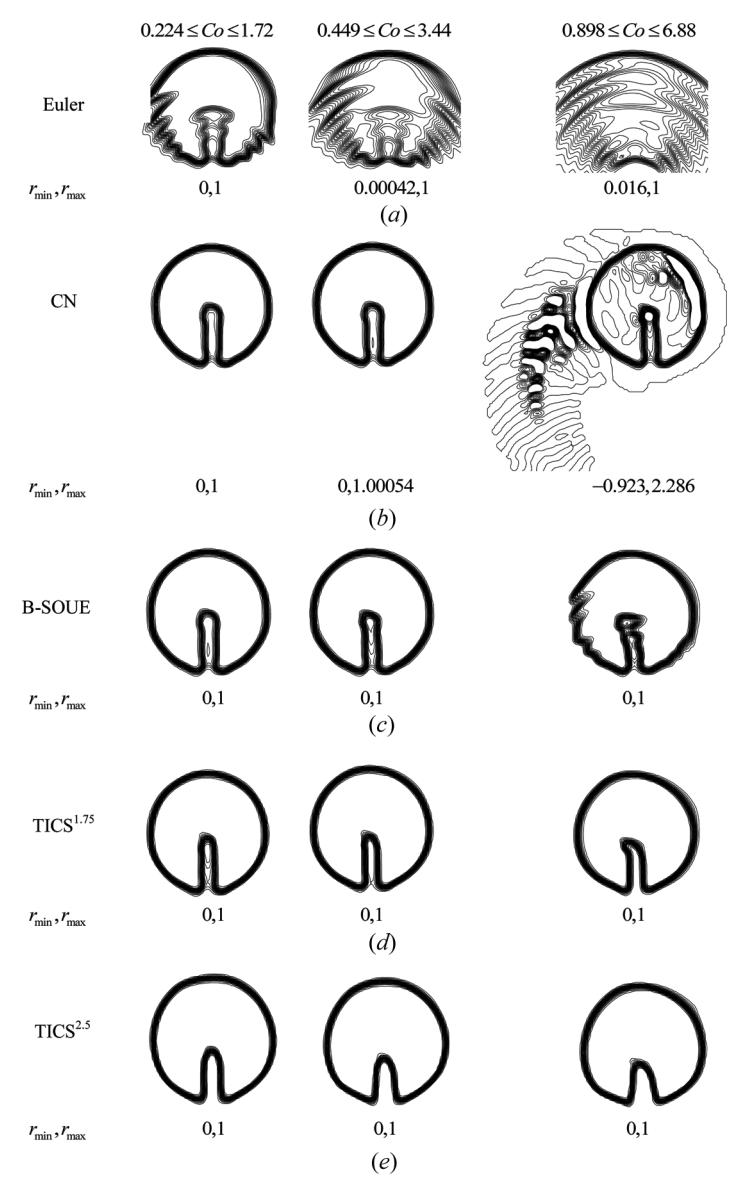


Figure 13. Contour plots of the r field for the advection in a rotational flow field of the slotted circle problem computed using the STACS advection scheme.

Advection of a Slotted Circle in a Rotational Flow Field

The rotation of a slotted circle around an external point is a difficult problem for advection schemes to solve, even though its exact solution is trivial [53, 54]. The computational domain considered here is a square with sides of length 4 m discretized into 200×200 (40,000) square computational cells, giving a control-volume of size $\Delta x = \Delta y = 5 \times 10^{-3}$ m. The circle of diameter 1 m has its center at (2, 2.65) m and is cut by a slot of width 0.12 m. The rotation of the slotted circle is driven by a vortex flow centered at the middle of the domain (2, 2) of angular velocity $\omega = 0.5 \, \text{rad/s}$. The time required by the slotted circle to complete a revolution is

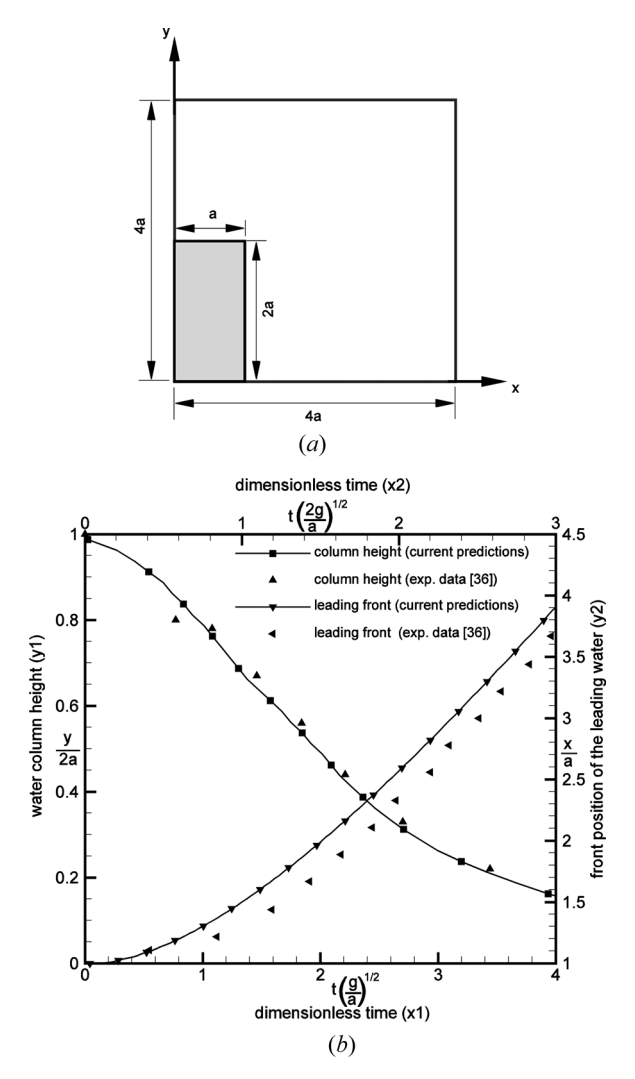


Figure 14. (a) Physical model of dam-break problem. (b) Comparison between numerical solutions and experimental results of the water column height and front position of the leading water for the brokendam problem.

 $2\pi/\omega$ s. With the geometry considered, the Courant number varies from a minimum (equal to $0.15 \times \omega \times \Delta t/\Delta x$) at point (2, 2.15) m to a maximum (equal to $1.15 \times \omega \times \Delta t/\Delta x$) at (2, 2.65) m. The problem is solved for three different local Courant number values such that the total period required for a revolution is subdivided into 840, 420, and 210 time steps, respectively. The exact solution for the problem is displayed in Figure 3d.

Contour plots for the *r* field generated using the SMART and STACS convective schemes with the various transient schemes are presented in Figures 12 and 13. As shown, the trend of results is similar to those presented earlier, with the sharper interfaces predicted when using the STACS convective scheme. The first-order Euler scheme profiles obtained with SMART (Figure 12*a*) are highly diffusive, whereas

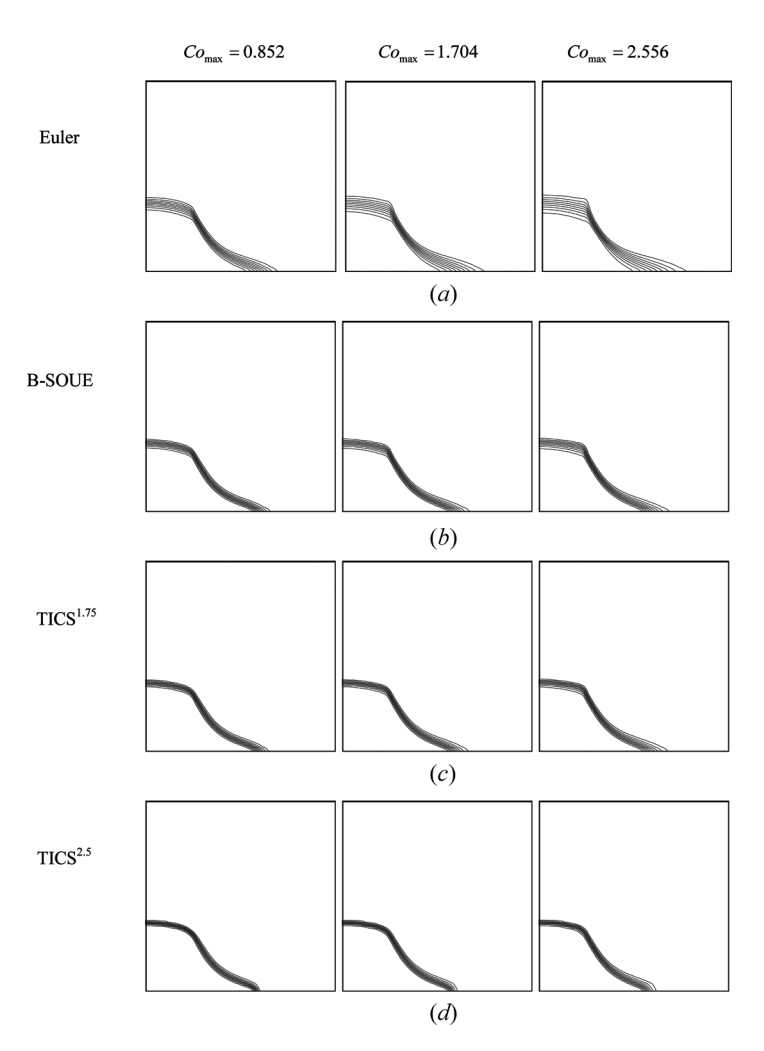


Figure 15. Contour plots of the r field for the collapse of a liquid column at time $t^* = 1.278$ computed using the SMART advection scheme.

profiles obtained with STACS are wiggly. Again, r values generated with the second-order CN scheme are unbounded (Figures 12b and 13b) at high values of Co, which limits the usefulness of the scheme to low Co values. Interfaces generated by the B-SOUE scheme (Figures 12c and 13c) are slightly more diffusive than the one obtained with the CN, however they are bounded at all Co values. This slight decrease in sharpness is the price that has to be paid for the scheme to remain bounded. The wiggles appearing at high Co in Figure 13c are due to the increase in false diffusion, as explained earlier. Profiles predicted by TICS^{1.75} (Figures 12d and 13d) and TICS^{2.5} (Figures 12e and 13e) are much sharper, with the sharpness increasing as m increases (i.e., sharper interfaces are obtained with TICS^{2.5}). Nevertheless, the shape of the slot is better preserved with the TICS^{1.75} scheme.

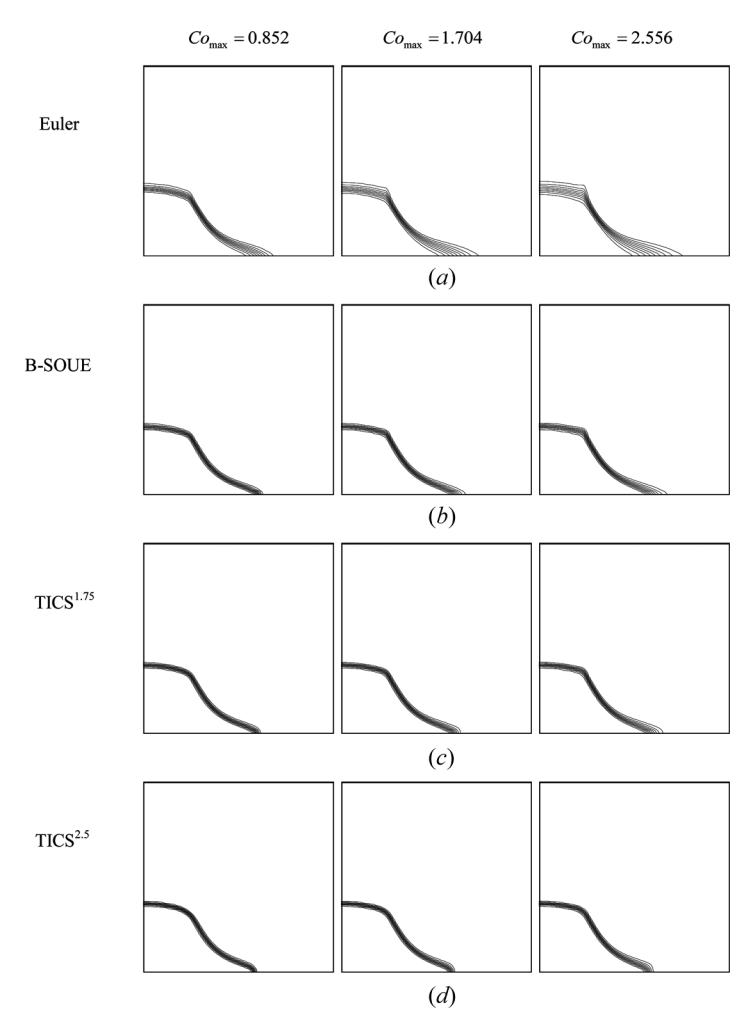


Figure 16. Contour plots of the r field for the collapse of a liquid column at time $t^* = 1.278$ computed using the STACS advection scheme.

The Dam-Break Problem

A schematic of the model is presented in Figure 14a. In this model, a column of water with width of $a=0.146\,\mathrm{m}$ and height 2a is located on the left side of a square tank with sides of size 4a filled with air. Water is considered viscous, with a constant density ρ_w and viscosity μ_w of values $998.2\,\mathrm{kg/m^3}$ and $0.993\times10^{-3}\,\mathrm{Pa\cdot s}$, respectively. Air is also considered to be of constant density and viscosity (ρ_a = $1.164\,\mathrm{kg/m^3}$, μ_a = $1.824\times10^{-5}\,\mathrm{Pa\cdot s}$). The water column, which is initially at rest, starts collapsing under its own weight at time t=0.

This problem differs from the previously presented problems in that the velocity field is not known *a priori*; rather, it is obtained as part of the solution. Therefore, in addition to the *r* equation, the momentum and continuity equations have to

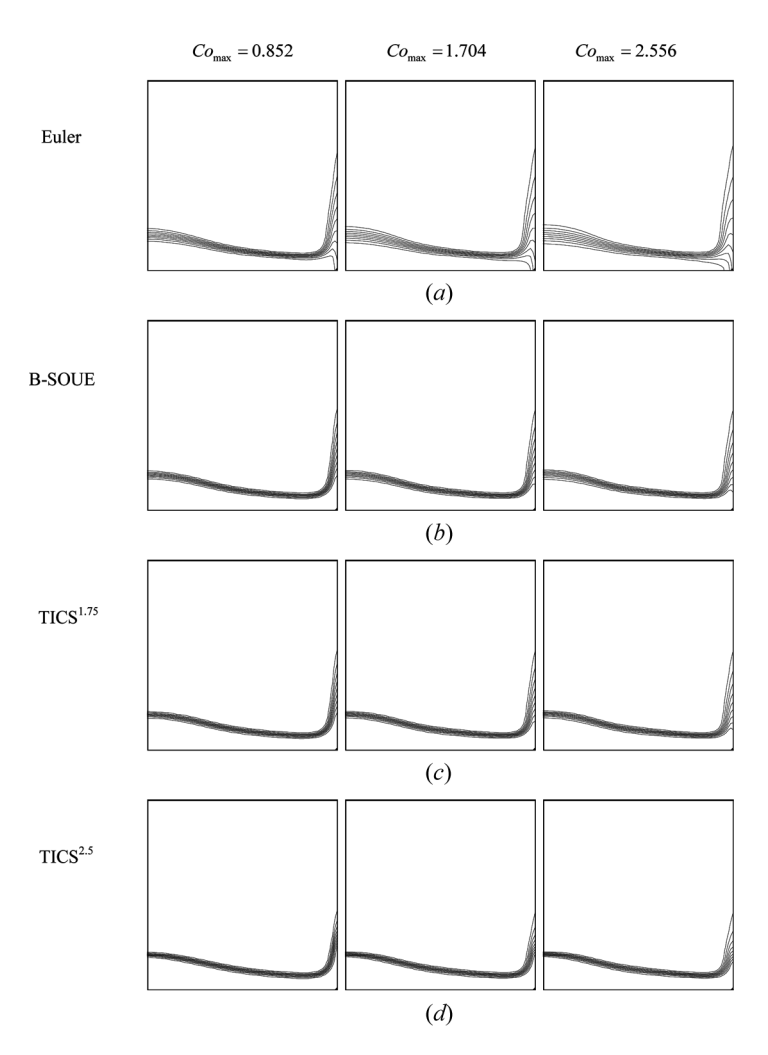


Figure 17. Contour plots of the *r* field for the collapse of a liquid column at time $t^* = 2.54$ computed using the SMART advection scheme.

be solved. The resulting flow field at time t>0 is modeled as laminar, the gravitational acceleration g is assigned the value of $9.8\,\mathrm{m/s^2}$, and surface tension effects are neglected. The boundary conditions are all set as no-slip wall conditions. The physical domain is subdivided into 80×80 control-volumes and the problem is solved for three different time steps, with values of $0.0026\,\mathrm{s}$, $0.0052\,\mathrm{s}$, and $0.0078\,\mathrm{s}$. With the maximum velocity not exceeding $\sqrt{2\times g\times(2a)}=2.392\,\mathrm{m/s}$, these time steps correspond to $\mathrm{Co_{max}}=0.852,\,1.704$, and 2.556, respectively. In the momentum equations, the convective terms are discretized using the SMART scheme, while the unsteady term is discretized via a first-order Euler scheme. In the r equation, however, the convective terms are discretized using either SMART or STACS, while the unsteady term is discretized using the various transient schemes presented earlier. Results are validated in Figure 14b by comparing the front position of the leading

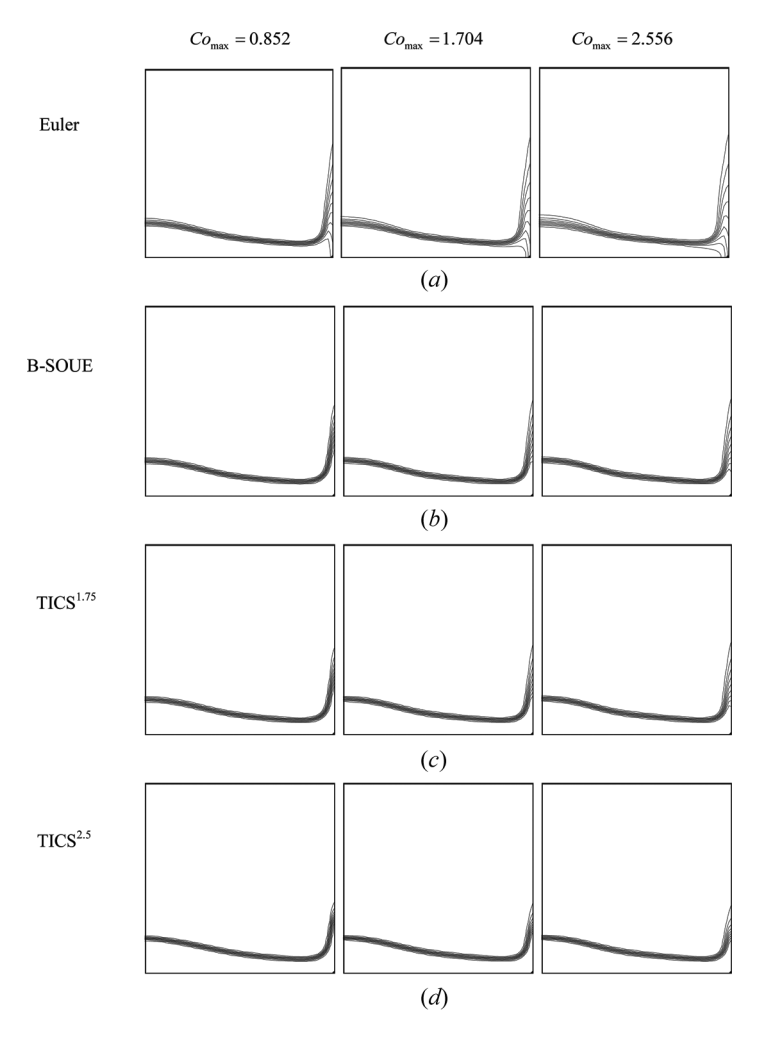


Figure 18. Contour plots of the *r* field for the collapse of a liquid column at time $t^* = 2.54$ computed using the STACS advection scheme.

water and the water column height predicted using STACS and TICS^{2.5} with experimental measurements reported by Martin and Moyce [55]. In the experimental results, the nondimensional times are different for the front position of the leading water and the water column height. The same nondimensional parameters are used here in the presentation of the numerical results to allow a direct comparison with the original publication [55]. As shown in Figure 14b, the column height values predicted numerically are very close to experimental data, while the front positions of the leading water calculations show a small deviation from the measurements. Similar deviations were reported in the literature (e.g., [56], with computations performed using the FLUENT commercial software) and may be due to the imperfect initial conditions in the experiments (e.g., nonuniform breaking of the diaphragm) and the physical effects not considered in the numerical model (e.g., surface tension).

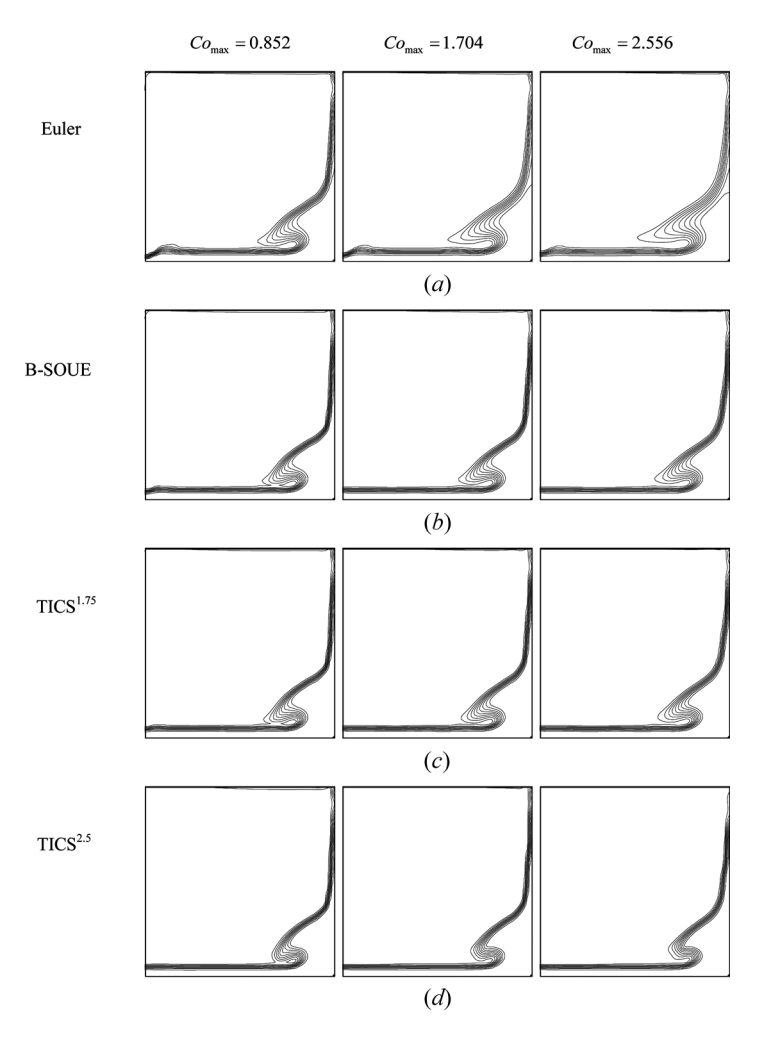


Figure 19. Contour plots of the *r* field for the collapse of a liquid column at time $t^* = 6$ computed using the SMART advection scheme.

Having established the credibility of the numerical procedure and calculation routines, solutions are generated for the various transient schemes using the SMART and STACS convective schemes; the results are presented in Figures 15–20. In all computations, results at any time step are assumed to be converged when the maximum absolute value of the residual of all variables falls below a small number ε_s set at 10^{-3} .

Contour plots of the r field generated by SMART are displayed in Figures 15, 17, and 19, while those generated by STACS are depicted in Figures 16, 18, and 20. In each of these Figures, solutions obtained using the first-order Euler (Figures 15a–20a), B-SOUE (Figures 15b–20b), TICS^{1.75} (Figures 15c–20c), and TICS^{2.5} (Figures 15d–20d) transient schemes at three values of the Co_{max} are presented.

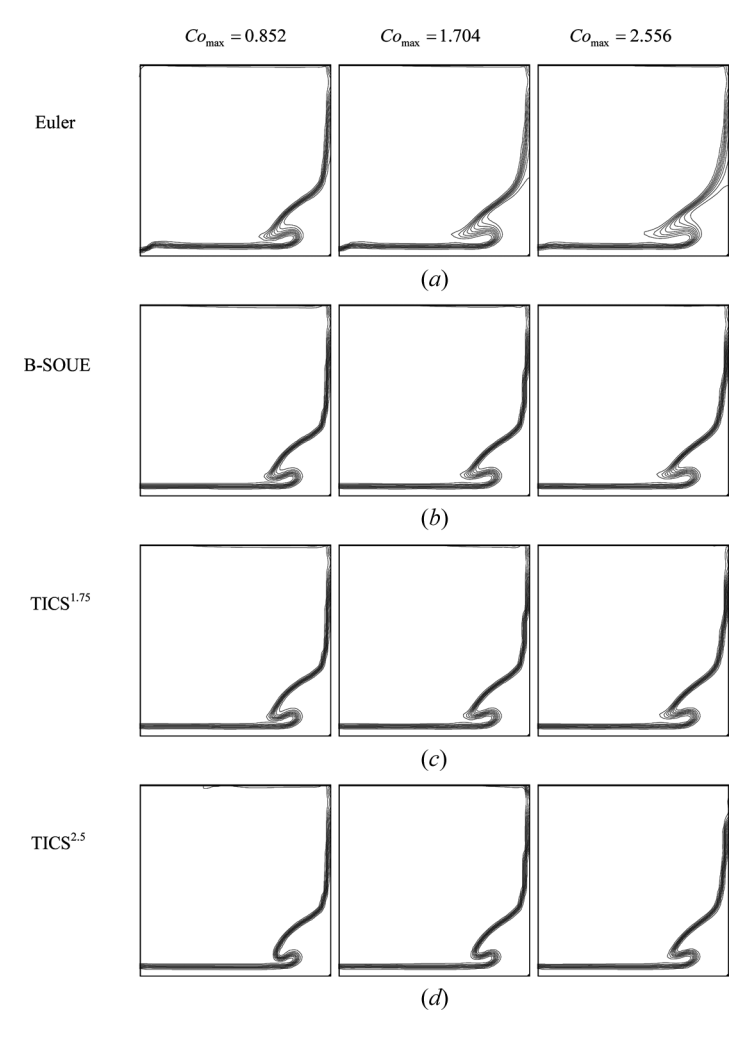


Figure 20. Contour plots of the *r* field for the collapse of a liquid column at time $t^* = 6$ computed using the STACS advection scheme.

Figures 15 and 16 show interfaces at the dimensionless time $t^* = t\sqrt{g/a} = 1.278$, Figures 17 and 18 at $t^* = 2.54$, and Figures 19 and 20 at $t^* = 6$. Computations using the CN scheme diverged after a certain number of time steps, not allowing results to be generated at the desired t^* values, with the time over which results could be obtained decreasing as Co_{max} increases. For this reason, no results using the CN scheme are presented.

The trend of results is similar to that presented earlier, with interfaces predicted by STACS (Figures 16, 18, and 20) being sharper than the corresponding ones obtained with SMART (Figures 15, 17, and 19) for all transient schemes, due to STACS being more compressive. Also, results become more diffusive, with a wider spread of the r contours around the interface, as Co_{max} increases. As with pure advection problems, the first-order Euler scheme is the most diffusive (Figures 15a–20a) at all Co_{max} and t^* values. Interfaces predicted by the TICS^{1.75} (Figures 15c–20c) scheme are slightly sharper than those obtained with the B-SOUE (Figures 15b–20b) scheme. This slight difference is due the fact that TICS^{1.75} (m=1.75) is slightly more compressive than B-SOUE (m=1.5). As shown in Figures 15d–20d, the sharpest interfaces at all Co_{max} and t^* values are those predicted by the TICS^{2.5} scheme. As seen in the plots, all schemes are capable of predicting the collapse of the water column on the left wall of the domain (t^* =1.278), the rise of water on the opposite side (t^* =2.54), and then its descent (t^* =6).

Again, by comparing contours obtained with the various schemes (Figures 15–20), it is clear that the performance of TICS^{2.5} is superior in preserving sharp interfaces.

CLOSING REMARKS

A new methodology for constructing transient interface-capturing schemes, given the acronym TICS, was presented. The TICS approach is based on a switching strategy that combines a bounded high-order transient scheme with a bounded transient compressive scheme. Bounded high-order and compressive transient schemes were constructed by discretizing the transient term over a temporal control-volume in a way similar to the discretization of the convective term. The TICS methodology was then applied to the bounded high-order and compressive transient schemes to create a new family of transient interface-capturing schemes that was designated by TICS^m. Two schemes (TICS^{1.75} and TICS^{2.5}) were used to demonstrate the virtues of the proposed methodology in preserving steep interfaces. The accuracy of the new transient TICS^m schemes was compared with the first-order Euler scheme, the Crank-Nicolson scheme, and the B-SOUE scheme by solving several test problems using the SMART and STACS convective schemes. Results demonstrated that interfaces obtained with TICS^{1.75} and TICS^{2.5} are sharper and bounded.

REFERENCES

 J. Ha, P. W. Cleary, V. Alguine, and T. Nguyen, Simulation of Die Filling in Gravity Die Casting Using SPH and MAGMA Soft, in *Proceedings of the Second International* Conference on CFD in the Minerals and Process Industries, Melbourne, Australia, 1999.

- 2. P. W. Cleary and J. Ha, Three-Dimensional Modeling of High Pressure Dies Casting, J. Cast Metals Res., vol. 12, pp. 357–365, 2000.
- 3. M. Darwish and F. Moukalled, Convective Schemes for Capturing Interfaces of Free-Surface Flows on Unstructured Grids, *Numer. Heat Transfer B*, vol. 49, pp. 19–42, 2006.
- 4. D. L. Youngs, An Interface Tracking Method for a 3D Eulerian Hydrodynamics Code, Tech. Rep. 44/92/35, Atomic Weapons Research Establishment, Harwell, UK, 1984.
- E. G. Puckett, A Volume of Fluid Interface Tracking Algorithm with Applications to Computing Shock Wave Rarefraction, in *Proceedings of the Fourth International* Symposium on Computational Fluid Dynamics, University of California at Davis, CA, 9–12 September, pp. 933–938, 1991.
- 6. S. O. Unverdi and G. Tryggvason, A Front Tracking Method for Viscous, Incompressible Multi-fluid Flow, *J. Comput. Phys.*, vol. 100, pp. 25–37, 1992.
- W. F. Noh and P. Woodward, (SLIC, Simple Line Interface Calculations), *Lecture Notes Phys.*, vol. 59, pp. 330–340, 1976.
- 8. M. Rudman, Volume Tracking Methods for Interfacial Flow Calculations, *Int. J. Numer. Meth. Fluids*, vol. 24, pp. 671–691, 1997.
- 9. Y. Renardy and M. Renardy, PROST: Parabolic Reconstruction of Surface Tension for the Volume-of-Fluid Method, *J. Comput. Phys.*, vol. 183, pp. 400–421, 2002.
- 10. Q. Chen, Y. Zhang, and M. Yang, An Interfacial Tracking Model for Convection-Controlled Melting Problems, *Numer. Heat Transfer B*, vol. 59, pp. 209–225, 2011.
- 11. D. Z. Guo, D. L. Sun, Z. Y. Li, and W. Q. Tao, Phase Change Heat Transfer Simulation for Boiling Bubbles Arising from A Vapor Film by the Voset Method, *Numer. Heat Transfer A*, vol. 59 pp. 857–881, 2011.
- 12. W. Lee, G. Son, and J. J. Jeong, Numerical Analysis of Bubble Growth And Departure From A Microcavity, *Numer. Heat Transfer, B*, vol. 58, no. 5, pp. 323–342, 2010.
- B. D. Nichols, C. W. Hirt, and R. S. Hotchkiss, SOLA-VOF: A Solution Algorithm for Transient Fluid Flow with Multiple Free Boundaries, Technical Report LA-8355, Los Alamos Scientific Laboratory, Los Alamos, NM, 1980.
- B. D. Nichols and C. W. Hirt, Methods for Calculating Multi-Dimensional, Transient Free-Surface Flows Past Bodies, in *Proceedings of the First International Conference of Numerical Ship Hydrodynamics*, Gaithersburg, ML, October 20–23, 1975.
- 15. C. W. Hirt and B. D. Nichols, Volume of Fluid (VOF) Method for the Dynamics of Free Boundaries, *J. Comput. Phys.*, vol. 39, pp. 201–225, 1981.
- F. H. Harlow and A. A. Amsden, Fluid dynamics: A LASA Monograph, LA-4700, Los Alamos National Laboratory, Los Alamos, NM, 1971.
- 17. B. Lafaurie, C. Nardone, R. Scardovelli, S. Zaleski, and G. Zanetti, Modeling Merging and Fragmentation in Multiphase Flows with SURFER, *J. Comput. Phys.*, vol. 113, pp. 134–147, 1994.
- V. Maronnier, M. Picasso, and J. Rappaz, Numerical Simulation of Free Surface Flows, J. Comput. Phys., vol. 155, pp. 439–455, 1999.
- D. B. Kothe, M. W. Williams, K. L. Lam, D. R. Korzekwa, P. K. Tubesing, and E. G. Puckett, A Second-Order Accurate, Linearity Preserving Volume Tracking Algorithm for Free-Surface Flows on 3-D Unstructured Meshes, in *Proceedings of the 3rd ASME, JSME Joint Fluids Engineering Conference*, San Francisco, CA, July 18–22, 1999.
- 20. J. U. Brackbill, D. B. Kothe, and C. Zemach, A Continuum Method for Modeling Surface Tension, *J. Comput. Phys.*, vol. 100, pp. 335–354, 1992.
- 21. D. B. Kothe and R. C. Mjolsness, RIPPLE: A New Model for Incompressible Flows with Free Surfaces, *AIAA J.*, vol. 30, pp. 2694–2700, 1992.
- 22. O. Ubbink and R. Issa, A Method for Capturing Sharp Fluid Interfaces on Arbitrary Meshes, *J. Comput. Phys.*, vol. 153, pp. 26–50, 1999.

- 23. Y. Suh, W. Lee, and G. Son, Bubble Dynamics, Flow, and Heat Transfer During Flow Boiling in Parallel Microchannels, *Numer. Heat Transfer A*, vol. 54, pp. 390–405, 2008.
- 24. J. D. Faires and R. L. Burden, Numerical Methods, PWS, Boston, pp. 152-153, 1993.
- J. Crank and P. Nicolson, A Practical Method for Numerical Evaluation of Solutions of Partial Differential Equations of the Heat-Conduction Type, *Proc. Cambr. Phil.* Soc., vol. 43, pp. 50–67, 1947.
- 26. W. Shyy, A Study of Finite Difference Approximations to Steady State Convection Dominated Flows, *J. Comput. Phys.*, vol. 57, pp. 415–438, 1985.
- 27. S. V. Patankar, Numerical Heat Transfer and Fluid Flow, Hemisphere, New York, 1981.
- 28. P. H. Gaskell and A. K. C. Lau, Curvature Compensated Convective Transport: SMART, a New Boundedness Preserving Transport Algorithm, *Int. J. Numer. Meth. Fluids*, vol. 8, pp. 617–641, 1988.
- 29. B. P. Leonard, A Stable and Accurate Convective Modeling Procedure Based on Quadratic Interpolation, *Comput. Meth. Appl. Mech. Eng.*, vol. 19, pp. 59–98, 1979.
- 30. C. T. DeGroot and A. G. Straatman, A Finite-Volume Model for Fluid Flow and Nonequilibrium Heat Transfer in Conjugate Fluid Porous Domains Using General Unstructured Grids, *Numer. Heat Transfer B*, vol. 60, pp. 252–277, 2011.
- 31. B. Hunter and Z. Guo, Comparison of the Discrete-Ordinates Method and the Finite-Volume Method for Steady-State and Ultrafast Radiative Transfer Analysis in Cylindrical Coordinates, *Numer. Heat Transfer B*, vol. 59, pp. 339–359, 2011.
- 32. L. Sun, S. R. Mathur, and J. Y. Murthy, An Unstructured Finite-Volume Method for Incompressible Flows with Complex Immersed Boundaries, *Numer. Heat Transfer B*, vol. 58, pp. 217–241, 2010.
- 33. S.-K. Choi and C.-L. Lin, A Simple Finite-Volume Formulation of the Lattice Boltzmann Method for Laminar and Turbulent Flows, *Numer. Heat Transfer B*, vol. 58, pp. 242–261, 2010.
- 34. M. M. Larmaei, J. Behzadi, and T.-F. Mahdi, Treatment of Checkerboard Pressure in the Collocated Unstructured Finite-Volume Scheme, *Numer. Heat Transfer B*, vol. 58, pp. 121–144, 2010.
- 35. F. Juretic and A. D. Gosman, Error Analysis of the Finite-Volume Method with Respect to Mesh Type, *Numer. Heat Transfer B*, vol. 57, pp. 414–439, 2010.
- 36. C. Kim, M. Y. Kim, M. J. Yu, and S. C. Mishra, Unstructured Polygonal Finite-Volume Solutions of Radiative Heat Transfer in a Complex Axisymmetric Enclosure, *Numer. Heat Transfer B*, vol. 57, pp. 227–239, 2010.
- 37. N. O. Moraga, S. Del, C. Ramirez, M. J. Godoy, and P. D. Ticchione, Study of Convective Non-Newtonian Alloy Solidification in Molds by the PSIMPLER/Finite-Volume Method, *Numer. Heat Transfer A*, vol. 57, pp. 936–953, 2010.
- 38. K. Guedri, M. Ammar Abbassi, M. Naceur Borjini, K. Halouani, and R. Said, Application of the Finite-Volume Method to Study the Effects of Baffles on Radiative Heat Transfer in Complex Enclosures, *Numer. Heat Transfer A*, vol. 55, pp. 780–806, 2009.
- 39. A. Dalal, V. Eswaran, and G. Biswas, A Finite-Volume Method for Navier-Stokes Equations on Unstructured Meshes, *Numer. Heat Transfer B*, vol. 54, pp. 238–259, 2008.
- 40. M. Y. Kim, S. W. Baek, and S. I. Park, Evaluation of the Finite-Volume Solutions of Radiative Heat Transfer in a Complex Two-Dimensional Enclosure with Unstructured Polygonal Meshes, *Numer. Heat Transfer B*, vol. 54, pp. 116–137, 2008.
- 41. P. Hassanzadeh and G. D. Raithby, Finite-Volume Solution of the Second-Order Radiative Transfer Equation: Accuracy and Solution Cost, *Numer. Heat Transfer B*, vol. 53, pp. 374–382, 2008.
- 42. R. Das, S. C. Mishra, and R. Uppaluri, Multiparameter Estimation in a Transient Conduction-Radiation Problem Using the Lattice Boltzmann Method and the

- Finite-Volume Method Coupled with the Genetic Algorithms, *Numer. Heat Transfer A*, vol. 53, pp. 1321–1338, 2008.
- 43. M. Ko and N. K. Anand, Three-Dimensional Combined Convective-Radiative Heat Transfer over a Horizontal Backward-Facing Step—A Finite-Volume Method, *Numer. Heat Transfer A*, vol. 54, pp. 109–129, 2008.
- 44. B. Mondal, S. C. Mishra, P. Asinari, and R. Borchiellini, Analysis of a Localized Fire in a 3-D Tunnel Using a Hybrid Solver: Lattice Boltzmann Method, Finite-Volume Method, and Fully Explicit Upwind Scheme, *Numer. Heat Transfer A*, vol. 53, pp. 392–417, 2008.
- 45. M. S. Darwish and F. Moukalled, Normalized Variable and Space Formulation Methodology for High-Resolution Schemes, *Numer. Heat Transfer B*, vol. 26, pp. 79–96, 1994.
- 46. W. Shyy, A Study of Finite Difference Approximations to Steady State Convection Dominated Flows, *J. Comput. Phys.*, vol. 57, pp. 415–438, 1985.
- 47. S. G. Rubin and P. K. Khosla, Polynomial Interpolation Method for Viscous Flow Calculations, *J. Comput. Phys.*, vol. 27, pp. 153–168, 1982.
- 48. J. D. Ramshaw and J. A. Trapp, Numerical Technique for Low Speed Homogeneous Two Phase Flow with a Sharp Interface, *J. Comput. Phys.*, vol. 21, pp. 438–453, 1976.
- 49. W. J. Rider and D. B. Kothe, Stretching and Tearing Interface Tracking Methods, AIAA Paper 95-1717 (Les Almos Natl. Lab. Rep. LA-UR-95-1145), presented at the 12th AIAA CFD Conference, San Diego, CA, June 19–22, 1995.
- 50. M. Rudman, Volume-Tracking Methods for Interfacial Flow Calculations, *Int. J. Numer. Meth. Fluids*, vol. 24, pp. 671–691, 1997.
- H. Jasak, Error Analysis and Estimation for the Finite Volume Method with Applications to Fluid Flows, Ph.D. thesis, Imperial College of Science, Technology and Medicine, London, 1996.
- 52. B. P. Leonard and H. S. Niknafs, Sharp Monotonic Resolution of Discontinuities without Clipping of Narrow Extrema, *Comput. Fluids*, vol. 19, pp. 141–154, 1991.
- 53. W. J. Rider and D. B. Kothe, Reconstructing Volume Tracking, *J. Comput. Phys.*, vol. 141, pp. 112–152, 1998.
- 54. S. T. Zalesak, Fully Multi-Dimensional Flux Corrected Transport Algorithms for Fluid Flow, *J. Comput. Phys.*, vol. 31, pp. 335–362, 1979.
- J. C. Martin and W. J. Moyce, An Experimental Study of the Collapse of Liquid Columns on a Rigid Horizontal Plane, *Phil. Trans. Roy. Soc. Lond., Ser. A*, vol. 244, pp. 312–324, 1952.
- 56. K. Abdolmaleki, K. P. Thiagarajan, and M. T. Morris-Thomas, Simulation of the Dam Break Problem and Impact Flows Using a Navier-Stokes Solver, *Proceedings of the 15th Australasian Fluid Mechanics Conference*, Paper # AFMC00031, Sydney, Australia, 13–17 December 2004.